J. Fluid Mech. (2009), *vol.* 628, *pp.* 269–297. © 2009 Cambridge University Press
doi:10.1017/S0022112009006193 Printed in the United Kingdom

Centrifugal effects in rotating convection: nonlinear dynamics

J. M. LOPEZ[1]† AND F. MARQUES[2]

[1]Department of Mathematics and Statistics, Arizona State University, Tempe, AZ 85287, USA

[2]Departament de Física Aplicada, Universitat Politècnica de Catalunya, Barcelona 08034, Spain

(Received 8 July 2008 and in revised form 18 January 2009)

Rotating convection in cylindrical containers is a canonical problem in fluid dynamics, in which a variety of simplifying assumptions have been used in order to allow for low-dimensional models or linear stability analysis from trivial basic states. An aspect of the problem that has received only limited attention is the influence of the centrifugal force, because it makes it difficult or even impossible to implement the aforementioned approaches. In this study, the mutual interplay between the three forces of the problem, Coriolis, gravitational and centrifugal buoyancy, is examined via direct numerical simulation of the Navier–Stokes equations in a parameter regime where the three forces are of comparable strengths in a cylindrical container with the radius equal to the depth so that wall effects are also of order one. Two steady axisymmetric basic states exist in this regime, and the nonlinear dynamics of the solutions bifurcating from them is explored in detail. A variety of bifurcated solutions and several codimension-two bifurcation points acting as organizing centres for the dynamics have been found. A main result is that the flow has simple dynamics for either weak heating or large centrifugal buoyancy. Reducing the strength of centrifugal buoyancy leads to subcritical bifurcations, and as a result linear stability is of limited utility, and direct numerical simulations or laboratory experiments are the only way to establish the connections between the different solutions and their organizing centres, which result from the competition between the three forces. Centrifugal effects primarily lead to the axisymmetrization of the flow and a reduction in the heat flux.

1. Introduction

One of the most fascinating aspects of rotating convection is the observation of spatio-temporal chaos essentially at the onset of convection as the Rayleigh number (non-dimensional imposed vertical temperature gradient) is increased (Krishnamurti 1971; Busse & Heikes 1980; Niemela & Donnelly 1986; Hu, Ecke & Ahlers 1997). This experimentally observed spatio-temporal chaos has been associated with the Küppers–Lortz (KL) instability (Küppers & Lortz 1969; Küppers 1970; Clever & Busse 1979). The KL instability occurs when the system is rotating faster than a critical level; convection rolls in a horizontally unbounded layer are unstable to rolls oriented at about 60°. The KL instability is formally found in an unbounded rotating system in the limit of zero centrifugal force. Experiments, of course, are conducted in bounded containers and most employ large horizontal-to-vertical aspect ratios.

† Email address for correspondence: lopez@math.asu.edu

https://doi.org/10.1017/S0022112009006193 Published online by Cambridge University Press

In the experiments, the switching in roll orientation occurs in patches throughout the layer and is characterized by both spatial and temporal irregularity (Hu *et al.* 1998). Reduced equation models have reproduced many aspects of the experimental observations (e.g. Busse & Heikes 1980; Tu & Cross 1992; Ponty, Passot & Sulem 1997), but for the most part these models are not derived directly from the governing hydrodynamic equations, Navier–Stokes–Boussinesq equations, and their dynamics can only be qualitatively compared with the experimental dynamics.

An aspect of the problem that has received only limited attention is the influence of the centrifugal force on the KL dynamics. One reason for this is that it is difficult (if not impossible) to derive an amplitude equation from the Boussinesq equations with the centrifugal force included, since this makes the Boussinesq equations inhomogeneous (Scheel 2007). Centrifugal buoyancy drives a large-scale circulation in which the cool denser fluid is centrifuged radially outwards and the warm less-dense fluid is centrifuged radially inwards (Barcilon & Pedlosky 1967; Homsy & Hudson 1969; Koschmieder 1993; Hart 2000). This large-scale circulation exists for any non-zero difference in temperature between the top and bottom plate. Neglecting the centrifugal buoyancy allows a straightforward linear stability analysis for the onset of convection from the conduction state; Chandrasekhar (1961) provides a comprehensive account of this for a horizontally unbounded fluid layer. However, the centrifugal buoyancy destroys the horizontal translation invariance that is inherent in the unbounded theoretical treatments of the problem, as well as the so-called Boussinesq reflection symmetry about the half-height of the layer (these idealizations neglecting centrifugal buoyancy are pervasive in models, e.g. Portegies *et al.* 2008). In one of the early experimental studies of rotating convection, Rossby (1967) states: 'When the apparatus is rotated, a radial acceleration, which increases with radius, is established.... However, since this radial acceleration destroys the horizontal uniformity, which is a basic assumption in the Bénard convection problem, it is essential that its influence be minimized. Obviously the radial acceleration cannot be eliminated entirely'.

Although most experimental studies are designed to keep the centrifugal force small compared to the gravitational force (e.g. Ning & Ecke 1993; Zhong, Ecke & Steinberg 1993; Bodenschatz, Pesch & Ahlers 2000), the experimental and numerical results of Becker *et al.* (2006) suggest that the centrifugal force may play a larger role than previously thought. While Becker *et al.* were able to compute a few isolated solutions with $F \neq 0$ in systems with large radius-to-depth aspect ratios of the order of 20, such computations are prohibitively expensive to conduct an extensive nonlinear analysis of the dynamics.

The ratio of centrifugal force to gravitational buoyancy is measured by the Froude number F, which is the reciprocal of a Richardson number (non-dimensional governing parameters are defined in § 2). In the limit of zero centrifugal buoyancy, Goldstein *et al.* (1993, 1994) studied the linear stability of the trivial basic state in finite cylinders. The linear stability of the non-trivial basic state incorporating centrifugal buoyancy in a finite cylinder has been analysed in the asymptotic limit of infinite Coriolis force and steady onset (Homsy & Hudson 1971). The linear stability analysis for finite values of the parameters and allowing for unsteady non-axisymmetric modes with radius-to-depth aspect ratio equal to one reveals that even for modest $F \sim 0.3$, the system admits numerous solution states that are heavily influenced by the centrifugal buoyancy (Marques *et al.* 2007). That analysis shows that for F sufficiently large, $F \gtrsim 0.4$, a state of axisymmetric large-scale circulation is stable and loses stability to a variety of three-dimensional modes as F is reduced.

https://doi.org/10.1017/S0022112009006193 Published online by Cambridge University Press

In the limit of $F \to 0$, the flow at sufficiently large Rayleigh numbers is complicated (a comprehensive overview of those linear results are presented in § 3, in order to put into context the new nonlinear three-dimensional dynamics presented in this paper). The nonlinear dynamics associated with the competition between gravitational buoyancy, Coriolis force and centrifugal buoyancy have not been systematically investigated previously. Linear stability analysis (Marques *et al.* 2007) and nonlinear axisymmetric simulations (Lopez, Rubio & Marques 2006) indicate that for Froude numbers as small as 0.05, the centrifugal force plays an important role leading to qualitative changes from the $F = 0$ case. The ratio of centrifugal force to gravitational buoyancy is measured by the Froude number, and the ratio of gravitational buoyancy to the Coriolis force is given by the thermal Rossby number (see § 2). For the most part, studies of rotating convection have finite Rossby numbers, but either the Froude number (ignoring centrifugal buoyancy) or the Richardson number is set to zero. The zero Richardson number has been studied extensively in the context of astrophysical convection (e.g. Busse 1970; Busse & Carrigan 1974; Busse 1994; Busse *et al.* 1998).

In this paper, the mutual interplay between the three forces – gravitational buoyancy, Coriolis and centrifugal – is examined via direct numerical simulation of the Navier–Stokes–Boussinesq equations. Section 2 describes the set-up of the problem and the numerical methods used. Section 3 summarizes the previous results in this problem of rotating convection in a cylinder of aspect ratio equal to one (Marques *et al.* 2007), where the two stable axisymmetric basic states (the so-called centrifugal and downwelling branches) and their linear stability were computed and analysed. In § 4 and § 5, the nonlinear dynamics of the solutions bifurcating from the centrifugal and downwelling branches are analysed. A variety of codimension-two bifurcation points is found. These points act as organizing centres for the dynamics. Section 6 summarizes the new nonlinear results and provides a global picture of all the solutions and their interacting dynamics. A main result is that the flow has simple dynamics at either low Rayleigh numbers (limit of gravitational buoyancy going to zero) or at large Froude numbers (limit of centrifugal buoyancy going to infinity), where the flow becomes steady and axisymmetric. With diminishing Froude number there is a cascade of subcritical bifurcations. In this parameter regime, all three forces are of comparable magnitude, and their competition and interaction leads to rich dynamics.

2. Governing equations and numerical scheme

Consider the flow in a circular cylinder of radius r_0 and depth d, rotating at a constant rate ω rad s^{-1}. The top endwall is maintained at a constant temperature $T_0 - 0.5\Delta T$ and the bottom endwall at a constant temperature $T_0 + 0.5\Delta T$, where T_0 is the mean temperature and ΔT is the temperature difference between the endwalls. There are five non-dimensional independent parameters:

$$\left.\begin{array}{ll} \text{Rayleigh number} & R = \alpha g d^3 \Delta T/(\kappa \nu), \\ \text{Coriolis number} & \Omega = \omega d^2/\nu, \\ \text{Froude number} & F = \omega^2 r_0/g, \\ \text{Prandtl number} & \sigma = \nu/\kappa, \\ \text{Aspect ratio} & \gamma = r_0/d, \end{array}\right\} \tag{2.1}$$

where α is the coefficient of volume expansion, g is the gravitational acceleration, κ is the thermal diffusivity and ν is the kinematic viscosity.

https://doi.org/10.1017/S0022112009006193 Published online by Cambridge University Press

With the problem depending on five non-dimensional parameters, a comprehensive parametric analysis is overwhelming. We have fixed $\gamma = 1$ to avoid very large azimuthal wavenumber modes, and $\sigma = 7.0$ which essentially corresponds to water near room temperature. We wish to analyse the relative importance of the gravitational buoyancy (characterized by R) and the centrifugal buoyancy (characterized by F) in a rotating system (the Coriolis acceleration being characterized by Ω). In a physical experiment, Ω and F vary simultaneously with the rotation frequency ω and either both are zero or both are different from zero. However, the classical treatment of the problem has been to take $F = 0$ and $\Omega \neq 0$, corresponding to the limit $g \to \infty$. Here, we fix $\Omega = 100$, and consider variations in R and F. In many studies of rotating convection, the Coriolis force is characterized by the Taylor number, $Ta = 2\Omega^2$, which for $\Omega = 100$ gives $Ta = 2 \times 10^4$.

Note that $Ri = 1/F$ is essentially a rotational Richardson number, giving the ratio of the gravitational potential energy to the rotational kinetic energy, and $Ro = (R/2\sigma\Omega^2)^{0.5}$ is a thermal Rossby number (Julien *et al.* 1996), giving the ratio of gravitational buoyancy to the Coriolis force squared. In the present study, $Ro \sim O(1)$ and $Ri \sim O(1)$, and so the three primary forces active in rotating convection are of comparable magnitudes and their nonlinear interactions and competition can be investigated.

The governing equations will be written in the rotating frame of reference, using the Boussinesq approximation: all fluid properties are considered constant, except for the density in the gravitational and centrifugal buoyancy terms. The validity of the Boussinesq approximation requires $\alpha\Delta T \ll 1$. Expressing this value in terms of the non-dimensional parameters of the problem we obtain

$$\alpha\Delta T = \frac{RF}{\sigma\Omega^2\gamma} = \frac{R}{\sigma Ga}, \qquad Ga = \frac{gd^3}{\nu^2}, \tag{2.2}$$

where Ga is the Galilei number of the fluid. For the values used in this study, $\alpha\Delta T \lesssim 10^{-1}$. For example, in the middle of the parameter region where Coriolis, centrifugal and gravitational buoyancy are of comparable strength, $Ra = 17\,000$ and $F = 0.33$ (see figure 21 for example), we find $\alpha\Delta T = 0.08$. $\alpha\Delta T$ can be made smaller by using larger Prandtl numbers, or increasing the Galilei number (for example, using larger convection cells or fluids with smaller kinematic viscosities), or both.

The governing equations, non-dimensionalized using d as the length scale, d^2/κ as the time scale, and ΔT as the temperature scale, are:

$$(\partial_t + \boldsymbol{u}\cdot\nabla)\boldsymbol{u} = -\nabla p + \sigma\nabla^2\boldsymbol{u} + \sigma R\Theta\hat{z} + 2\sigma\Omega\,\boldsymbol{u}\times\hat{z} - \tfrac{\sigma FR}{\gamma}(\Theta - z)\boldsymbol{r}, \tag{2.3}$$

$$(\partial_t + \boldsymbol{u}\cdot\nabla)\Theta = w + \nabla^2\Theta, \qquad \nabla\cdot\boldsymbol{u} = 0. \tag{2.4}$$

where $\boldsymbol{u}$ is the velocity field in the rotating frame, (u, v, w) are the components of $\boldsymbol{u}$ in cylindrical coordinates (r, θ, z), p is the kinematic pressure (including gravitational and centrifugal contributions), $\hat{z}$ the unit vector in the vertical direction z and $\boldsymbol{r}$ is the radial vector in cylindrical coordinates. Instead of the non-dimensional temperature T, we have used the temperature deviation Θ with respect to the conductive profile, $T = T_0/\Delta T - z + \Theta$, as is customary in many thermal convection studies. The boundary conditions for $\boldsymbol{u}$ and Θ are:

$$r = \gamma: \qquad \Theta_r = u = v = w = 0, \tag{2.5}$$

$$z = \pm 1/2: \quad \Theta = u = v = w = 0. \tag{2.6}$$

https://doi.org/10.1017/S0022112009006193 Published online by Cambridge University Press

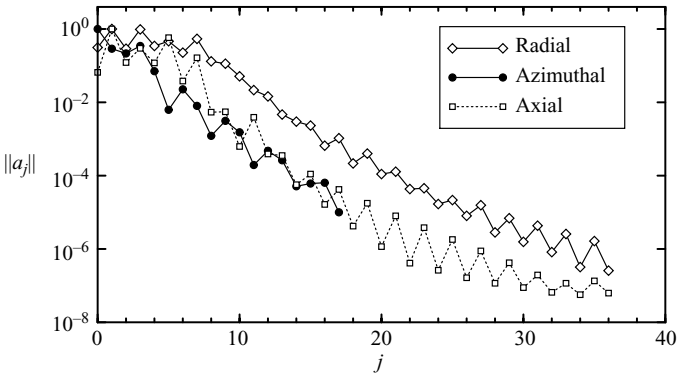


FIGURE 1. Convergence of the spectral coefficients (2.7) of the radial velocity using the infinity norm. The flow corresponds to a quasi-periodic solution at $R = 19.500$ and $F = 0.30$, computed with $L = 36$ Chebyshev radial points, $M = 18$ Fourier modes and $N = 36$ Chebyshev axial points.

The governing equations are invariant under rotations around the axis of the cylinder. If the Froude number is zero, the governing equations are also invariant to a reflection K_z about the half-height $z = 0$, whose action is $K_z(u, v, w, \Theta, p)(r, \theta, z) = (u, v, -w, -\Theta, p)(r, \theta, -z)$. This so-called Boussinesq symmetry is broken by the centrifugal term, and plays only a role when F is zero or very small.

The governing equations have been solved using the second-order time-splitting method proposed in Hughes & Randriamampianina (1998) combined with a pseudo-spectral method for the spatial discretization, utilizing a Galerkin–Fourier expansion in the azimuthal coordinate θ and Chebyshev collocation in $x = r/\gamma$ and $y = 2z$:

$$F(r, \theta, z) = \sum_{l=0}^{L} \sum_{n=0}^{N} \sum_{m=-M}^{M} a_{l,n,m} T_l(x) T_n(y) \mathrm{e}^{\mathrm{i}m\theta}. \tag{2.7}$$

The velocity components, temperature and pressure are the real or imaginary parts of F. The radial dependence of the variables is approximated by Chebyshev expansions with appropriate parities of their azimuthal Fourier component (Fornberg 1998). To avoid including the origin in the collocation mesh, an odd number of Gauss–Lobatto points in r is used and the equations are solved only in the interval $r \in (0, \gamma]$. Following Orszag & Patera (1983), we have used the combinations $u_+ = u + \mathrm{i}v$ and $u_- = u - \mathrm{i}v$ in order to decouple the linear diffusion terms in the momentum equations. For each Fourier mode, the resulting Helmholtz equations for Θ, w, u_+ and u_- have been solved using a diagonalization technique in the two coordinates r and z. The imposed parity of the Fourier modes guarantees the regularity conditions at the origin needed to solve the Helmholtz equations (Mercader, Net & Falqués 1991). We have used $L = N = 36$ spectral modes in r and z, $M = 18$ in θ and a time step $dt = 2 \times 10^{-5}$ thermal time units in all computations. We have checked the spectral convergence of the code using the infinity norm of the spectral coefficients of the computed solutions, defined as $||a_l||_\infty = \max_{n,m} |a_{l,n,m}|$ for the radial direction, and analogously for the axial and azimuthal directions. Figure 1 shows $\|a_j\|_\infty$, with $j = l, n, m$, of the radial velocity u for a quasi-periodic solution at $R = 19\,500$ and $F = 0.30$, one of the most

https://doi.org/10.1017/S0022112009006193 Published online by Cambridge University Press

complex solutions obtained. The trailing coefficients of the spectral expansion (2.7) are at least five orders of magnitude smaller than the leading coefficients.

To describe the state of the system, we use the mid-cylinder temperature,

$$\Theta_m = \Theta(r = 0, \theta = 0, z = 0), \tag{2.8}$$

as it discriminates well between the different branches of solutions. Another useful set of characteristics are the energies (L_2-norms) of the azimuthal Fourier modes of a given solution,

$$E_m = \frac{1}{2} \int_{z=-1/2}^{z=1/2} \int_{r=0}^{r=\gamma} \boldsymbol{u}_m \cdot \boldsymbol{u}_m^* \, r \, \mathrm{d}r \, \mathrm{d}z \,, \tag{2.9}$$

where $\boldsymbol{u}_m$ is the mth Fourier mode of the velocity field and $\boldsymbol{u}_m^*$ is its complex conjugate. They aid in monitoring the relative influence of, and switching between, different modes during temporal evolution. To describe the heat transfer properties of a solution we use the Nusselt number, the ratio between the heat transfer of the solution considered and the heat transfer of the conductive state, both through the top lid. It is given by

$$Nu = -\frac{1}{\pi\gamma^2} \int_{r=0}^{r=\gamma} \int_{\theta=0}^{\theta=2\pi} \frac{\partial T}{\partial z}\Big|_{z=0.5} r \, \mathrm{d}r \, \mathrm{d}\theta \,. \tag{2.10}$$

Time-dependent solutions are also characterized by their frequencies. When a steady solution undergoes a Hopf bifurcation to a rotating wave with azimuthal wavenumber m, the imaginary part of the critical eigenvalue is the Hopf frequency ω_H. This Hopf frequency is closely related to the precession frequency ω_p of the rotating wave, defined as the angle through which the pattern rotates per unit time: $\omega_p = \omega_H/m$. The dependence of any dynamic variable of a rotating wave on θ and t is of the form $f(\theta - \omega_p t)$. When this variable is Fourier expanded in θ, the phase ϕ_m in the mth Fourier mode changes by an amount $\Delta\phi_m = m\omega_p \Delta t$ in a time Δt. By computing this phase shift at every (r, z) point of the computational domain, we have a large set of ω_p values. The mean of these values is the ω_p value we accept, and the variance σ_{ω_p} is a measure of how close our state is to a rotating wave. This method can be applied to any time-dependent solution, giving different precession frequencies for every Fourier mode, with the corresponding variance. These values have proved useful in the analysis of quasi-periodic solutions.

2.1. *Bifurcation curves*

In the present study a large variety of nonlinear solutions and bifurcation curves between them have been computed; they are listed in the Appendix. The steady axisymmetric states and their bifurcation curves were computed in Marques *et al.* (2007) using arclength continuation and linear stability analysis (Lopez, Marques & Sanchez 2001; Sanchez, Marques & Lopez 2002). The bifurcated solutions, which are time periodic, have been computed by time evolution; by restricting the computations to appropriate subspaces, it has also been possible to compute some of their unstables branches. These periodic solutions undergo secondary bifurcations; when the critical eigenvectors belong to an orthogonal Fourier subspace, the eigenvalues and eigenvectors have been computed with the time evolution code, and the critical point is obtained by bisection and linear interpolation. This method is more efficient than using continuation and linear stability analysis of periodic solutions (via Krylov methods), which is not very practical for large partial differential equation (PDE) systems because of the difficulties of having an efficient preconditioner (Barkley, Gomes &

https://doi.org/10.1017/S0022112009006193 Published online by Cambridge University Press

Henderson 2002), and because these methods demand higher precisions (increasing the number of spectral modes and the computational cost) than time evolution (Barkley *et al.* 2002; Nore *et al.* 2003). When the bifurcations are supercritical (Hopf and pitchfork type) it is also possible to locate the bifurcation point using the normal form estimate of the amplitude of the bifurcated solutions, fitting their amplitudes to $\sqrt{|R - R_{crit}|}$. We have used all of these techniques when possible, and used results from time evolution and dynamical systems theory when nothing else was available and efficient. For example, to our knowledge, there are no available continuation and linear stability methods for quasi-periodic solutions of PDE with 2×10^5 degrees of freedom, as is the case in the present problem.

3. Axisymmetric solutions manifold

The axisymmetric solutions and their stability to arbitrary perturbations were computed and analysed in Marques *et al.* (2007). In this section, we summarize the main results to put into context the new nonlinear three-dimensional dynamics discussed in this paper.

In the absence of centrifugal buoyancy ($F = 0$), the basic state is the conductive state where the fluid is in solid-body rotation with a linear vertical temperature profile: $\Theta = 0$ and $\boldsymbol{u} = 0$. For non-zero Froude number, the basic state is more complex; for any non-zero temperature difference, $R \neq 0$, the cool fluid near the top of the cylinder is centrifuged radially outwards while the warm fluid close to the bottom is centrifuged radially inwards, generating a large-scale circulation and a nonlinear vertical temperature profile. Note that in the convectively stable situation ($R < 0$), with $F \neq 0$, the centrifugal buoyancy also drives a similar large-scale circulation, but with the sense of the circulation reversed; the warm fluid near the top of the cylinder is centrifuged radially inwards while the cool fluid close to the bottom is centrifuged radially outwards (Brummell, Hart & Lopez 2000). For the aspect ratio considered, $\gamma = 1$, a single axisymmetric recirculation cell results, whose strength increases with increasing Froude number.

Figure 2(a) shows isotherms of Θ, plotted in a meridional plane and in a horizontal section at mid-height for a steady axisymmetric centrifugal solution $C0$, at $R = 2 \times 10^4$ and $F = 0.4$. This solution connects smoothly with the zero solution at $R = 0$, and is stable over a wide region in parameter space (the large light-grey shaded region in figure 3). As well as $C0$, there are many additional axisymmetric steady solutions; for example, up to seven different such solutions have been found at $R = 2.0 \times 10^4$ and $F = 0.1$ (Marques *et al.* 2007). However, most of these solutions are unstable, and there is only one additional stable steady axisymmetric solution (for some parameter values). An example is plotted in figure 2(b) at $R = 1.6 \times 10^4$ and $F = 0.4$. It is very similar to $C0$, except that it has a downwelling cold plume on the axis; we call this branch the downwelling branch $D0$. The $D0$ solutions are only stable in the narrow triangular region depicted in figure 3.

The linear stability of the $C0$ and $D0$ solutions has been determined in Marques *et al.* (2007), and figure 3 shows the corresponding bifurcation curves delimiting the stability regions of the two branches. The centrifugal branch becomes unstable at Hopf bifurcations to rotating waves with azimuthal wavenumbers $m = 3$ (for moderate Rayleigh numbers, $R \leqslant 2.010 \times 10^4$) and $m = 2$ (for larger Rayleigh numbers, $R \geqslant 2.010 \times 10^4$). At the codimension-two point $(R, F) \approx (2.010 \times 10^4, 0.3000)$, $C0$ becomes simultaneously unstable to both rotating waves; this is a double-Hopf bifurcation dH_{23}. $D0$ is born at a saddle-node bifurcation curve, the long left-hand

https://doi.org/10.1017/S0022112009006193 Published online by Cambridge University Press

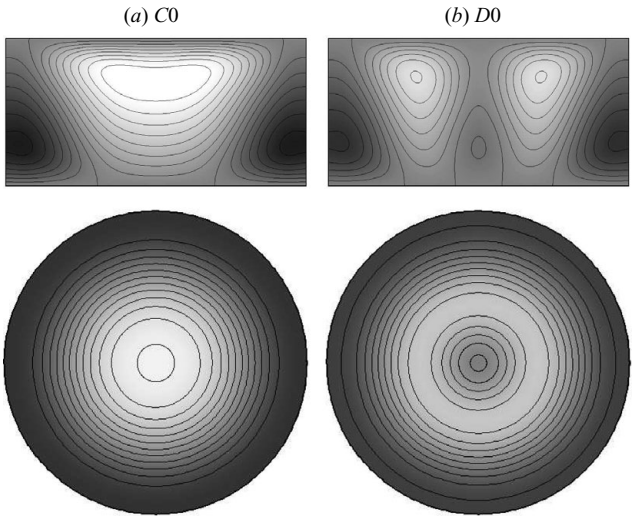


FIGURE 2. Contour plots of temperature deviation Θ on a meridional plane (top row) and at mid-height (bottom row), corresponding to (*a*) the centrifugal branch $C0$ at $R = 2.0 \times 10^4$ and (*b*) the downwelling branch $D0$ at $R = 1.6 \times 10^4$, both at $F = 0.4$. There are eight positive and eight negative contour levels, in the range $\Theta \in [-0.4, 0.4]$, with black being the most negative and white the largest positive in the grey scale.

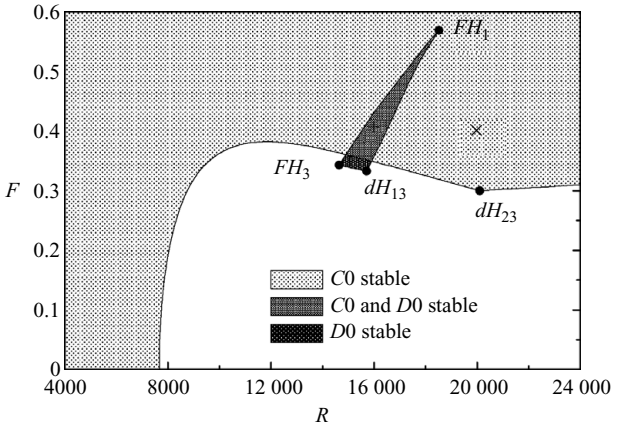


FIGURE 3. Regime diagram for the stable axisymmetric solutions; in the white region only three-dimensional solutions are stable, in the large light-grey shaded region only $C0$ is stable, in the small rectangular region only $D0$ is stable and in the triangular region both $C0$ and $D0$ are stable. The $C0$ solution plotted in figure 2(*a*) is at the $\times$ symbol and the $D0$ solution plotted in figure 2(*b*) is at the + symbol.

side of the narrow triangle in figure 3. The downwelling branch becomes unstable at Hopf bifurcations to rotating waves with azimuthal wavenumbers $m = 3$ (for moderate Rayleigh numbers, $R \leqslant 1.572 \times 10^4$) and $m = 1$ (for larger Rayleigh numbers, $R \geqslant 1.572 \times 10^4$). The two rotating waves bifurcate simultaneously at the double-Hopf bifurcation dH_{13} at $(R, F) \approx (1.572 \times 10^4, 0.3328)$. The Hopf bifurcation curves meet the saddle-node curve at two fold-Hopf codimension-two bifurcations, FH_1 and FH_3, at $(R, F) \approx (1.852 \times 10^4, 0.5693)$ and $(R, F) \approx (1.465 \times 10^4, 0.3430)$, respectively. The eigenmodes corresponding to the Hopf bifurcations are wall modes, i.e. the maximum

https://doi.org/10.1017/S0022112009006193 Published online by Cambridge University Press

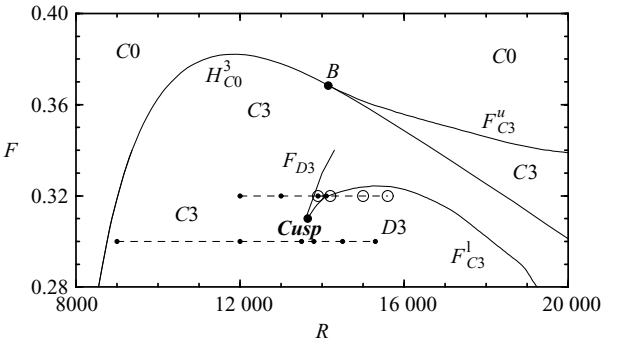


FIGURE 4. Bifurcations of the centrifugal branch $C0$, showing the Hopf bifurcation to the rotating wave $C3$, H^3_{C0}, which is supercritical for small R up to the Bautin point B where it becomes subcritical and from where a fold bifurcation of $C3$, F^u_{C3}, emanates. The $C3$ solution manifold is folded at a cusp point *Cusp*, from which two fold bifurcation curves emanate, F_{D3} and F^l_{C3}. The symbols on the two horizontal dashed line at $F=0.32$ and $F=0.30$ are the locations of the various states illustrated in figure 5.

values of the temperature and velocity perturbations are located near the sidewall. There is one exception, the $m=1$ Hopf bifurcation of $D0$ (the curve connecting FH_1 and dH_{13}). In this case the eigenvector has the maximum values near the axis, it is a precession mode of the downwelling central plume (see Marques *et al.* 2007). The details of the various three-dimensional flow structures are presented below along with the analyses of the bifurcated states and their secondary bifurcations.

4. Bifurcations of the centrifugal branch

As F is reduced and R is increased, the axisymmetric solutions lose stability to three-dimensional bifurcations in a myriad of ways (glossaries of the solution states and the associated bifurcations are provided in the Appendix). In the following sections, these are treated individually and described in detail, and finally a global picture of how they are inter-connected is presented.

4.1. *C3 manifold of solutions*

At low Rayleigh number, the centrifugal branch $C0$ becomes unstable at a supercritical Hopf bifurcation to a rotating wave $C3$ with azimuthal wavenumber $m=3$. The Hopf bifurcation curve H^3_{C0} is nearly independent of F for small F, but for large F the centrifugal effects become important, and the Hopf curve bends towards larger R. At $(R, F)\approx(14157, 0.3684)$, the Hopf bifurcation H^3_{C0} becomes subcritical at a codimension-two degenerate Hopf bifurcation, called a Bautin bifurcation B (Kuznetsov 2004) which is also known as a generalized Hopf bifurcation (Guckenheimer & Holmes 1997). The most salient feature of this bifurcation is the existence of an unstable $C3$ when the bifurcation is subcritical, that becomes stable at a saddle-node bifurcation curve F^u_{C3}. This curve meets the Hopf bifurcation curve H^3_{C0} tangentially at the Bautin point B. The loci of the various bifurcations in (R, F) space are shown in figure 4. On decreasing F, the rotating wave solution $C3$, born at the saddle-node bifurcation curve F^u_{C3}, loses stability at another saddle-node bifurcation curve F^l_{C3}. Between the two saddle-node curves, $C3$ is stable. The saddle-node bifurcation curve F^l_{C3} originates at a cusp bifurcation *Cusp* located

https://doi.org/10.1017/S0022112009006193 Published online by Cambridge University Press

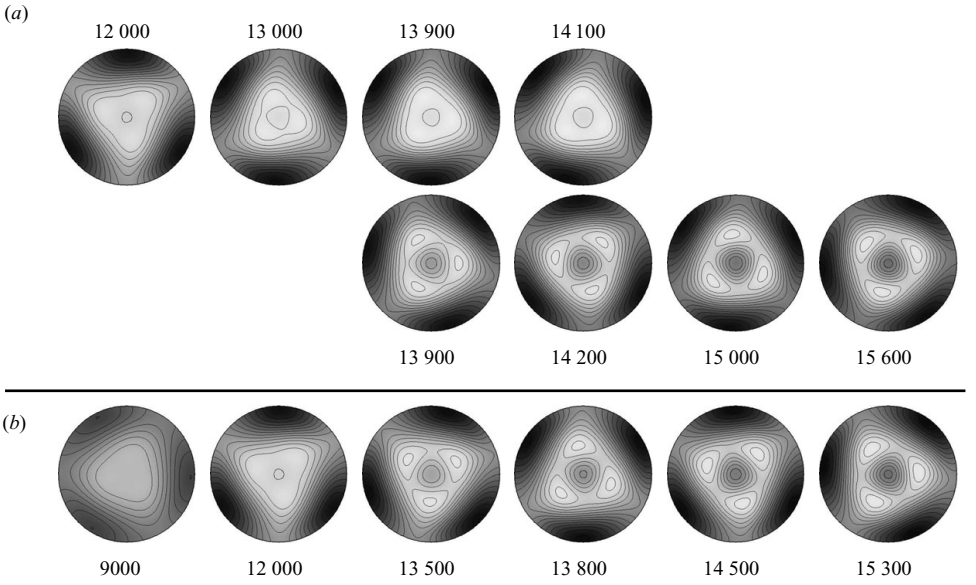


FIGURE 5. Contours of temperature deviation Θ at mid-height $z = 0$; there are eight positive and eight negative contour levels, in the range $\Theta \in [-0.3, 0.3]$, with black being the most negative and white the largest positive in the grey scale. Part (a) corresponds to solutions on the $C3$ branch (top row) and the $D3$ branch (bottom row) at $F = 0.32$ and R as indicated, while part (b) corresponds to a smooth transition from $C3$ to $D3$ at $F = 0.30$ as R is varied as indicated. The loci of these solution in (R, F) space are indicated in figure 4.

at $(R, F) \approx (13650, 0.31)$. The variation in the flow structure of $C3$ solutions in a neighbourhood of the cusp bifurcation is shown in figure 5. The first two rows (figure 5a) show the upper and lower solution branches of the cusp at $F = 0.32$. There is coexistence inside the horn region originating at the cusp point. The cusp and the two fold bifurcations emanating from it, F_{D3} and F^l_{C3}, are also shown in figure 4, where the loci of the solutions on the upper branch are shown as bullets •. These are typical $C3$ states, with a wide hot plume rising in the middle of the cylinder. The loci of solutions on the lower branch are shown as circles ○ in figure 4, and close to the sidewall they are identical to the $C3$ states, but they have an additional downwelling cold plume in the centre of the cell. These states are identical to the states bifurcating from the downwelling axisymmetric state $D0$, and we call them $D3$. Their relationship with the bifurcations of the $D0$ branch will be analysed in § 5. For Froude numbers below the cusp point, there is no hysteresis but only a single branch undergoing a smooth transition between the $C3$ and $D3$ states. This smooth transition as R is increased is illustrated in figure 5(b) at $F = 0.3$, and their corresponding loci are also shown in figure 4 as bullets •.

The formation of the cusp bifurcation is illustrated in figure 6(a) showing how the mid-cylinder temperature Θ_m for $C2$ varies with R for different F. Below the cusp ($F < 0.31$), there is a smooth transition between $C3$ (relatively warm Θ_m) and $D3$ (relatively cool Θ_m) as R is increased. At $F = 0.31$, the Θ_m curve develops a vertical slope, and for $F > 0.31$ the curve is multivalued; only the two stable branches of each curve are shown. The end points of these curves are saddle-node bifurcations, their loci in (R, F) space are illustrated in figure 4 as the fold bifurcation curves F^l_{C3} (where $C3$ becomes unstable) and F_{D3} (where $D3$ becomes unstable). The fate of

https://doi.org/10.1017/S0022112009006193 Published online by Cambridge University Press

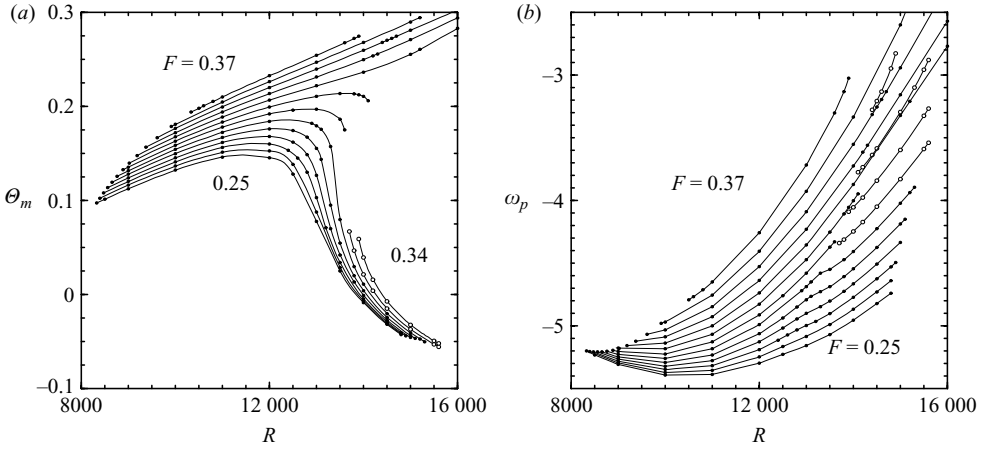


FIGURE 6. Rotating wave solutions $C3$, characterized by (a) the mid-cylinder temperature Θ_m and (b) the precession frequency ω_p, plotted as functions of R, for $F \in [0.25, 0.37]$ in steps of 0.01. Computed solutions are indicated by symbols • and ○.

the F_{D3} is associated to the bifurcations of the $D0$ branch, and will be explored in § 5. Figure 6(b) shows the precession frequency ω_p as a function of R for different F values; ω_p is retrograde and decreases in absolute value when R increases. These curves also illustrate the formation of the *Cusp* bifurcation.

4.2. *C2 manifold of solutions*

At large R, $C0$ becomes unstable to a rotating wave $C2$ with azimuthal wavenumber $m = 2$, rather than the $m = 3$ rotating wave $C3$ at low R, as F is reduced. The exchange of critical azimuthal mode from 3 to 2 occurs at a double-Hopf point dH_{23} at $(R, F) \approx (20\,098, 0.30002)$. At a double-Hopf bifurcation, two different periodic solutions and a quasi-periodic mixed mode bifurcate simultaneously. Additional more complicated solutions may also appear, including three-torus heteroclinic connections and chaotic horns, depending on the particulars of the problem (Kuznetsov 2004). At the double-Hopf bifurcation dH_{23}, the two Hopf bifurcation curves H^2_{C0} and H^3_{C0} that meet at dH_{23} are subcritical Hopf bifurcations. As a result, in a neighbourhood of dH_{23} where normal form analysis is valid, the only stable state is $C0$ (stable for F above the two Hopf curves, see figure 3). In fact, what we observe in a neighbourhood of dH_{23} are the two rotating waves $C2$ and $C3$ that coexist and are stable. They become stable at saddle-node bifurcation curves, F^u_{C3} and F_{C2}, due to the subcritical nature of the Hopf bifurcations. These states are far away in phase space from the neighbourhood of the double-Hopf dH_{23} where the normal form analysis is valid.

The $C2$ states exist in a wide region of (R, F) space below the saddle-node bifurcation curve F_{C2}, as shown in figure 7. At low R, along the curve labelled sH_{C2} in figure 7, the rotating waves $C2$ undergo a secondary Hopf bifurcation sH_{C2} where they lose stability. This secondary Hopf bifurcation is subcritical and there are no stable states in the neighbourhood of sH_{C2} (other than $C2$ on the high-R side of the curve). Following the bifurcation, evolutions initiated near the unstable $C2$ state evolve to the (remote in phase space) $D3$ states, described in § 4.1 and in figure 4.

https://doi.org/10.1017/S0022112009006193 Published online by Cambridge University Press

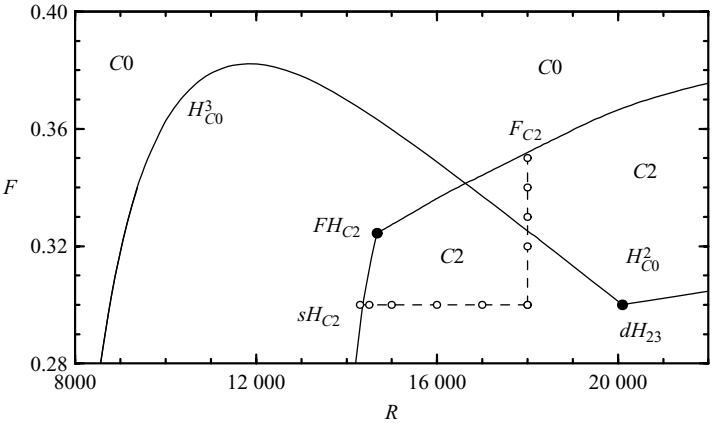


FIGURE 7. Bifurcations of the rotating wave $C2$, showing the double-Hopf point dH_{23} where the two Hopf bifurcation curves H^2_{C0} and H^3_{C0} meet, the fold bifurcation curve F_{C2} and the secondary Hopf bifurcation curve sH_{C2} that meet at the fold-Hopf point FH_{C2}. The symbols on the two dashed lines are the loci of the various $C2$ states shown in figure 8.

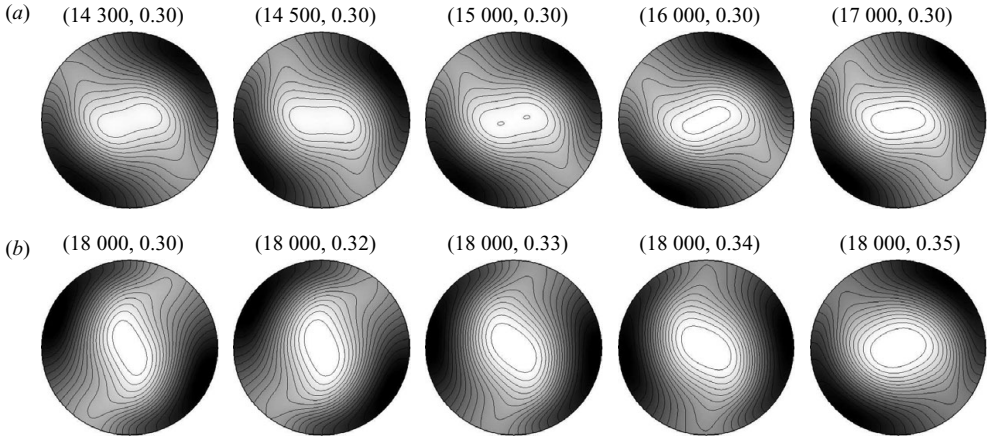


FIGURE 8. Solutions on the $C2$ branch. Contours of temperature deviation Θ at mid-height $z=0$; there are 8 positive and 10 negative contour levels, in the range $\Theta \in [-0.3, 0.3]$. Part (a) corresponds to solutions at $F=0.30$ and R as indicated, while part (b) corresponds to solutions at $R=18\,000$ as F is varied as indicated.

The structure of the rotating waves $C2$ is shown in figure 8. The first row corresponds to the symbols in the horizontal dashed line at $F=0.30$ in figure 7, starting at the secondary Hopf curve sH_{C2}. The second row corresponds to the symbols in the vertical dashed line at $R=18000$ in figure 7, terminating at the saddle-node curve F_{C2}. The structure of the $C2$ solutions does not change very much in their region of stability; the most noticeable change being the shape of the wide central hot plume that becomes more elongated on approaching the secondary Hopf curve sH_{C2}, while becoming more circular on approaching the saddle-node curve F_{C2}.

The codimension-two fold-Hopf bifurcation admits distinct dynamic scenarios. A comprehensive description of these scenarios is given in Kuznetsov (2004). The FH_{C2} bifurcation we have found belongs to the simplest case in which there exists only

https://doi.org/10.1017/S0022112009006193 Published online by Cambridge University Press

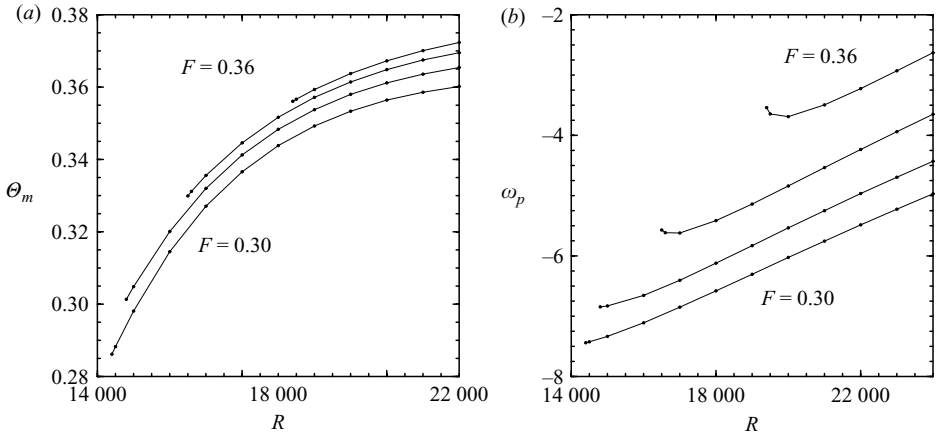


FIGURE 9. Rotating wave solutions $C2$, characterized by (a) the mid-cylinder temperature Θ_m and (b) the precession frequency ω_p, plotted as functions of R, for $F \in [0.30, 0.36]$ in steps of 0.02. Computed solutions are indicated by the symbols •.

one stable state, a fixed point born at the saddle-node curve F_{C2} that becomes unstable at the Hopf curve sH_{C2}. Although in our problem $C2$ is a periodic solution and the fold-Hopf normal-form theory applies to fixed points, rotating waves are relative equilibria (fixed points in the appropriate rotating reference frame) and their normal-form analysis is identical to that of fixed points.

Figure 9(a) shows how the mid-cylinder temperature Θ_m for $C2$ varies with R for different F. Θ_m increases with increasing R, tending to saturate at high-R values. Figure 9(b) shows the precession frequency ω_p as a function of R for different F values; it is retrograde with respect to the rotation of the cylinder, and increases almost linearly with R in the parameter range considered. For high-F values, the C2 solution is born at the saddle-node bifurcation curve F_{C2}, and ω_p departs from the linear behaviour close to this bifurcation.

Figure 10 summarizes the bifurcations of the centrifugal branch $C0$ analysed in the previous sections. The rotating waves $C2$ and $C3$ coexist and are stable in a wide parameter region bounded by the curves F^u_{C3}, F_{C2} and F^l_{C3}. They also coexist with the stable steady state $C0$ above the two Hopf curves emerging from dH_{23}. Which one of these three states is observed in an experiment or in a numerical simulation depends on initial conditions and the path followed in parameter space.

5. Bifurcations of the downwelling branch

5.1. *D3 Manifold of solutions*

At low Rayleigh numbers $R \leqslant 1.572 \times 10^4$, the downwelling branch $D0$ becomes unstable in a supercritical Hopf bifurcation to a rotating wave $D3$ with azimuthal wavenumber $m = 3$. The Hopf bifurcation curve H^3_{D0} exists in a small parameter region, and is limited by two codimension-two bifurcations: the fold-Hopf bifurcation FH_3, where the Hopf bifurcation curve H^3_{D0} meets the saddle-node curve F_{D0} (where the axisymmetric downwelling state $D0$ is born), and the double-Hopf point dH_{13}, as shown in figure 11. The $D3$ solutions have already been found at low Froude number, where the $C3$ branch undergoes a smooth transition to $D3$ with increasing R, as illustrated in figure 5(b) at $F = 0.30$. For larger Froude number, $C3$ and $D3$ coexist

https://doi.org/10.1017/S0022112009006193 Published online by Cambridge University Press

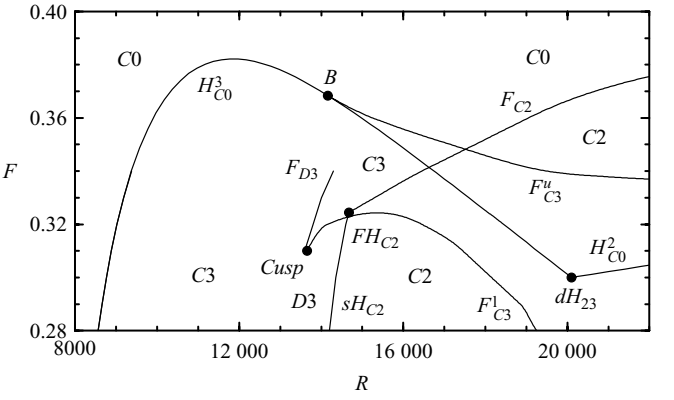


FIGURE 10. Regime diagram summarizing the bifurcations of the centrifugal branch. $C0$ becomes unstable at the two Hopf bifurcation curves emerging from the double-Hopf point dH_{23}. These Hopf curves are subcritical to the right of the Bautin point B. $C3$ develops a central cold plume at low F, evolving into a $D3$ rotating wave; this is organized by the *Cusp* point. Finally, $C2$ becomes unstable at low R along the secondary Hopf curve sH_{C2}, that meets F_{C2} at the codimension-two FH_{C2} point. The codimension-two bifurcation points are indicated by the symbols •.

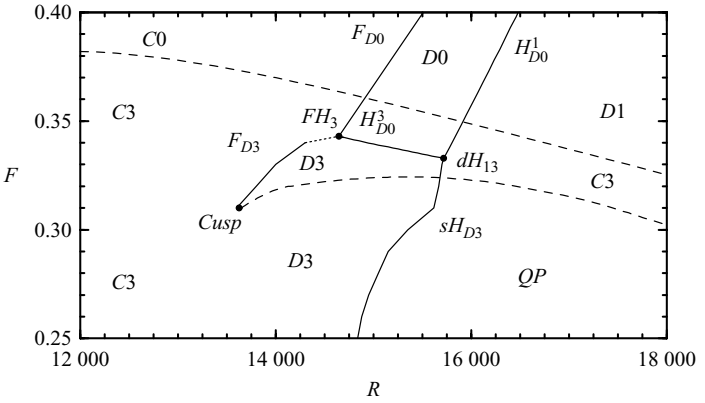


FIGURE 11. Bifurcations of the rotating wave $D3$, born at the Hopf curve H_{D3}. At low R disappears in the fold bifurcation F_{D3}, while at large R becomes unstable in the secondary Hopf sH_{D3}, where a quasi-periodic solution emerges. At low R and F, below the *Cusp* point, $D3$ smoothly becomes a $C3$ state.

in a hysteresis region close to the cusp bifurcation, also illustrated in figure 5(a) at $F = 0.32$.

The fold-Hopf codimension-two bifurcation FH_3 (see figure 11) is the collision of a saddle-node bifurcation (F_{D0}) and a Hopf bifurcation (H^3_{D0}). As described in many standard texts on dynamical systems (Guckenheimer & Holmes 1997; Kuznetsov 2004), from a fold-Hopf point emerges a secondary Hopf bifurcation curve where the periodic solution ($D3$ in our case) looses stability in a supercritical bifurcation. However, in our problem the $D3$ state disappears in a fold bifurcation of cycles F_{D3}. This means that the supercritical secondary Hopf emerging from FH_3 becomes subcritical very close to the fold-Hopf point. Consequently, in a neighbourhood of FH_3 the rotating wave $D3$ has four eigenvalues with real part very close to zero: two

https://doi.org/10.1017/S0022112009006193 Published online by Cambridge University Press

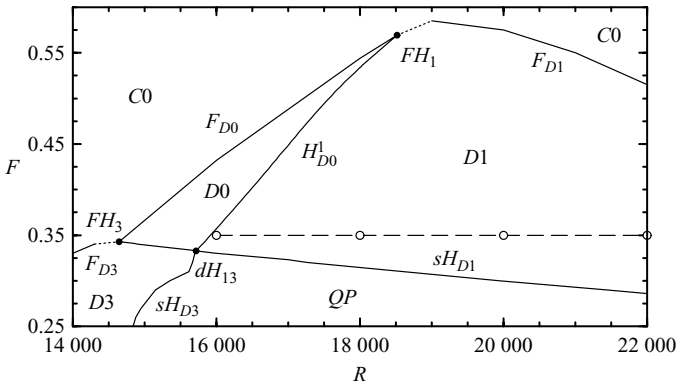


FIGURE 12. Bifurcations of the rotating wave $D1$, showing the Hopf bifurcation curve H^1_{D0} where $D1$ is born, and the fold curve F_{D1} and the secondary Hopf curve sH_{D1} where $D1$ becomes unstable. These curves meet at the codimension-two points FH_1 and dH_{13}. The symbols on the dashed line are the loci of the $D1$ states shown in figure 13.

zero eigenvalues associated to the two saddle-node curves F_{D0} and F_{D3}, and the pair of complex conjugates eigenvalues associated to the Hopf curve H^3_{D0}. The presence of so many eigenvalues very close to zero makes it almost impossible to compute solutions very close to the fold-Hopf point due to the extremely slow decay of transients. We have represented the unexplored connection of the saddle-node curve F_{D3} with the fold-Hopf point FH_3 as a dotted line.

Increasing R at constant F, the rotating waves $D3$ undergo a supercritical secondary Hopf bifurcation along the curve labelled sH_{D3} in figure 11. This curve emerges from the double-Hopf point dH_{13}. A description of the double-Hopf bifurcation and the quasi-periodic states emerging at the secondary Hopf bifurcation is presented in § 5.3.

5.2. *D1 Manifold of solutions*

For Rayleigh numbers $R \geqslant 1.572 \times 10^4$, the downwelling branch $D0$ becomes unstable in a supercritical Hopf bifurcation to a rotating wave $D1$ with azimuthal wavenumber $m = 1$. The Hopf bifurcation curve H^1_{D0} is bounded by two codimension-two bifurcations: the fold-Hopf bifurcation FH_1, where the Hopf bifurcation curve H^1_{D0} meets the saddle-node curve F_{D0} where the axisymmetric downwelling state $D0$ is born, and the double-Hopf point dH_{13}, as shown in figure 12. The previous rotating waves obtained at Hopf bifurcations from the axisymmetric base states $C0$ and $D0$ are all wall modes ($C2$, $C3$ and $D3$) with the perturbation forming alternating hot and cold plumes near the sidewall. The rotating wave $D1$ born at H^1_{D0} is associated with a different physical mechanism: it is a jet instability of the central cold plume characteristic of the downwelling axisymmetric state $D0$. This central plume is displaced from the centre of the cell, and precesses around the cylinder axis. The structure of the $D1$ solutions can be seen in figure 13, showing four solutions along the path $F = 0.35$, indicated as • in figure 12. The first solution, at $R = 1.6 \times 10^4$, is very close to the supercritical Hopf H^1_{D0}, the displacement of the central plume is small and the flow is close to axisymmetric. The displacement of the plume and the non-axisymmetric nature of $D1$ increases with increasing R.

Figure 14(a) shows the mid-cylinder temperature Θ_m and the precession frequency ω_p on the $D1$ branch, plotted as a function of R, for different Froude numbers F. The temperature in the centre of the cell increases with R because as the amplitude

https://doi.org/10.1017/S0022112009006193 Published online by Cambridge University Press

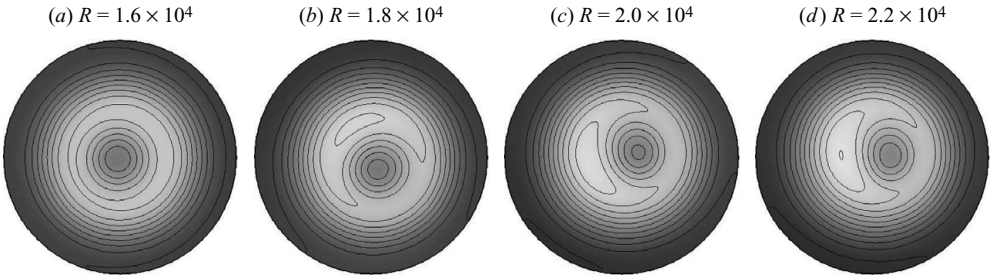


FIGURE 13. Snap shots of Θ for the $D1$ rotating waves at $F = 0.35$ and R as indicated. There are 8 positive and 8 negative contour levels, in the range $\Theta \in [-0.4, 0.4]$, with black being the most negative and white the largest positive in the grey scale.

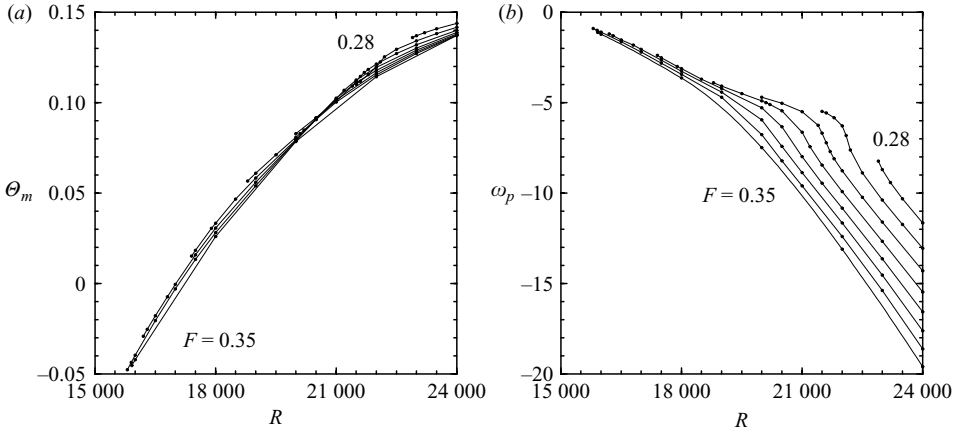


FIGURE 14. Rotating wave solutions $D1$, characterized by (a) the mid-cylinder temperature Θ_m and (b) the precession frequency ω_p, plotted as functions of R, for $F \in [0.28, 0.35]$ in steps of 0.01. Computed solutions are indicated by the symbols •.

of the precession of the central plume increases, the cold spot moves away from the centre, as can be observed in figure 11. The precession of the $D1$ rotating waves is retrograde and increases with R, as shown in figure 14(b).

Increasing the Froude number, the rotating waves $D1$ disappear in a saddle-node bifurcation F_{D1}. In exactly the same manner as discussed in § 5.1, a supercritical secondary Hopf bifurcation where the periodic solution $D1$ loses stability emerges from the fold-Hopf bifurcation point FH_1. This secondary Hopf bifurcation becomes subcritical and very close to the fold-Hopf point, resulting in the emergence of the saddle-node curve F_{D1}. With so many eigenvalues very close to zero in this regime, it is almost impossible to compute solutions very close to the fold-Hopf point FH_1. We have represented the unexplored connection of the saddle-node curve F_{D1} with the fold-Hopf point as a dotted line in figure 12.

Decreasing F at constant R, the rotating waves $D1$ undergo a subcritical secondary Hopf bifurcation along the curve labelled sH_{D1} in figure 12. This curve emerges from the double-Hopf point dH_{13}. A description of the double-Hopf bifurcation and the quasi-periodic states emerging at the secondary Hopf bifurcation is presented in the following section.

https://doi.org/10.1017/S0022112009006193 Published online by Cambridge University Press

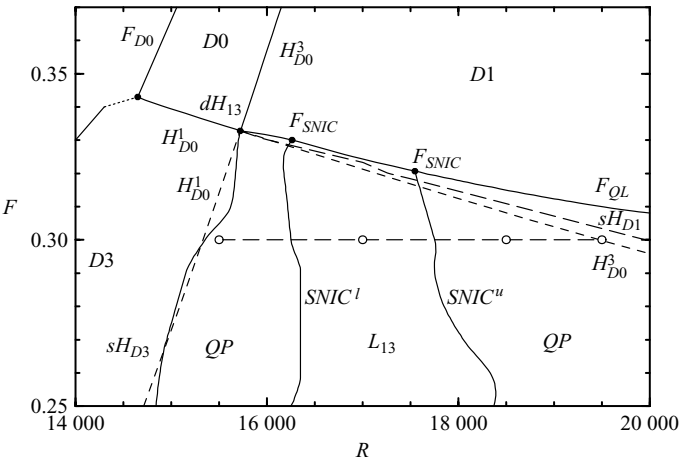


FIGURE 15. From the double-Hopf bifurcation dH_{13}, a stable quasi-periodic solution QP emerges. QP disappears at large F in a fold bifurcation of tori, F_{QL}. At low R undergoes a secondary Hopf bifurcation sH_{D3} becoming a $D3$ rotating wave. Between the two SNIC curves, QP becomes a locked mixed-mode L_{13}, a rotating wave solution. The symbols on the dashed line are the loci of the $D1$ states shown in figure 16.

5.3. *Double-Hopf bifurcation* dH_{13}

The double-Hopf bifurcation dH_{13} plays a central role in the organization of the dynamics of the downwelling branch solutions. As shown in figure 15, a number of different bifurcation curves meet at dH_{13}: the two Hopf curves, H^1_{D0} and H^3_{D0}, and the two secondary Hopf curves sH_{D1} and sH_{D3} (these have already been described earlier), as well as a saddle-node curve of quasi-periodic solutions (not yet analysed). From the different scenarios of the double-Hopf bifurcation described in standard textbooks (e.g. Kuznetsov 2004), the precise scenario corresponding to dH_{13} cannot be found. This is due to exactly the same reason as has already been observed in the two fold-Hopf bifurcations FH_1 and FH_3: the secondary Hopf bifurcation curves emerging from these codimension-two points are supercritical, but they become subcritical very close to the codimension-two point. As a result, the normal-form analysis is valid only in a very narrow parameter region around the double-Hopf point; this type of behaviour has been observed in diverse dynamical problems (Wittenberg & Holmes 1997). Although the codimension-two points play a central role as organizing centres for the dynamics, in a real problem the dynamics may differ very quickly from the dynamics predicted by the local normal-form analysis. This problem has been generally observed with many reduced low-dimensional models (normal forms, Ginzburg–Landau equations, etc.). Although these models are very useful because they predict the different states that emerge from a given bifurcation, only the solution of the full problem (direct numerical simulation of the Navier–Stokes equations in our case) can produce the global picture, the interconnections between the different organizing centres, and determine the region of validity of the reduced models (e.g. see Lopez, Marques & Shen 2004).

The double-Hopf dH_{13} corresponds to the simple scenario described in Kuznetsov (2004), termed type II. In the region delimited by the secondary Hopf curves sH_{D1} and sH_{D3}, the rotating waves $D1$ and $D3$ are both unstable and a quasi-periodic mixed-mode QP is stable. Very close to dH_{13} the curve sH_{D1} is supercritical, and the precise point where it becomes subcritical and the saddle-node of quasi-periodic

https://doi.org/10.1017/S0022112009006193 Published online by Cambridge University Press

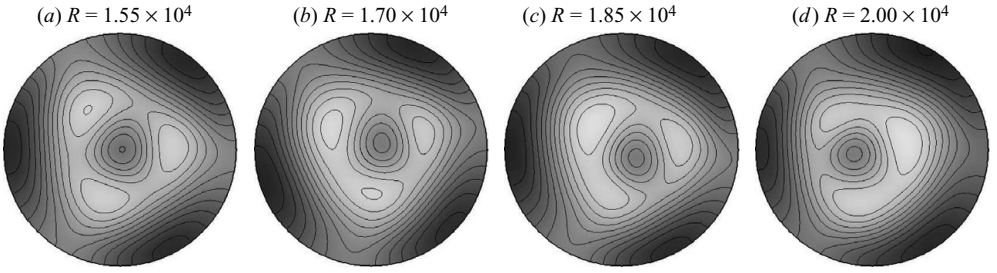


FIGURE 16. Snap shots of Θ for the mixed-mode solutions at (*a*) $R = 1.55 \times 10^4$ (QP), (*b*) $R = 1.70 \times 10^4$ (L_{13}), (*c*) $R = 1.85 \times 10^4$ (QP) and (*d*) $R = 2.00 \times 10^4$ (QP), all at $F = 0.30$. There are eight positive and eight negative contour levels, in the range $\Theta \in [-0.4, 0.4]$, with black being the most negative and white the largest positive in the grey scale. The loci of these solution in (R, F) space are indicated in figure 15. The movies available on-line animate these solutions.

solutions F_{QL} is born has not been determined, for the same reasons as in the fold-Hopf bifurcations FH_1 and FH_3. The connection between sH_{D1}, F_{QL} and dH_1 shown in figure 15 is purely schematic.

The QP state is a mixed mode originating at the double-Hopf bifurcation for $D1$ and $D3$. The region of existence is delimited by the secondary Hopf curves. The QP state has the $m = 1$ and $m = 3$ components quite well separated in physical space, since the $m = 3$ component primarily corresponds to the $D3$ 'wall mode' state and $D1$ is a precession mode of the $D0$ axial plume. The structure of the mixed mode can be observed in figure 16, showing the plumes close to the wall and the central plume precessing off-centre (the mixed-mode dynamics can be fully appreciated in the online movies). The loci in (R, F) space of the four snapshots of QP are indicated by the symbols $\circ$ on the dashed line in figure 15.

5.4. *Locking on the QP*

The quasi-periodic QP synchronizes to a mixed-mode solution whose $m = 1$ and $m = 3$ Fourier components are locked to the same precession frequency L_{13}, between the two curves labelled $SNIC^l$ and $SNIC^u$ in figure 15. The synchronized L_{13} is robust and stable over an extensive region of parameter space, with $1.6 \times 10^4 < R < 1.8 \times 10^4$ and $F < 0.33$ (at least down to the smallest $F = 0.25$ which has been systematically explored here), as illustrated in figure 15. The bifurcation from QP to L_{13} is a saddle-node-on-an-invariant-circle (SNIC) bifurcation. Figure 17(*a*) is a schematic diagram of a SNIC bifurcation. Before the bifurcation there exists a stable limit cycle. At the bifurcation a saddle-node appears on the cycle. After the bifurcation the saddle-node splits into two fixed points, one stable and the other unstable, destroying the limit cycle (its remnants are the stable and unstable manifolds of the two fixed points). In our problem, we do not have a limit cycle, but a quasi-periodic solution on a two torus; but the dynamics on a Poincaré section of the torus is the same as the dynamics just described for the SNIC bifurcation, as illustrated in figure 17(*b*): before the SNIC bifurcation, there is a a quasi-periodic solution whose intersections with the Poincaré section produce an invariant cycle. The intersection points of a quasi-periodic orbit with the Poincaré section drift on the invariant cycle, densely filling it. After the SNIC bifurcation, a pair of synchronized periodic states, one stable (L_{13}) and the other unstable, correspond to the stable and unstable fixed points on the Poincaré section.

https://doi.org/10.1017/S0022112009006193 Published online by Cambridge University Press

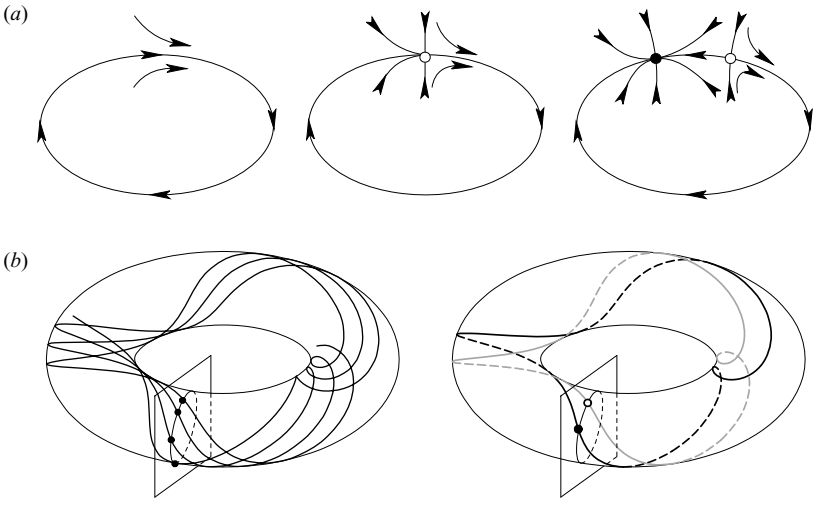


FIGURE 17. (*a*) Schematic diagram of a SNIC bifurcation. (*b*) Schematic diagram of a SNIC bifurcation on a two-torus; the Poincaré section depicted displays the behaviour described in (*a*).

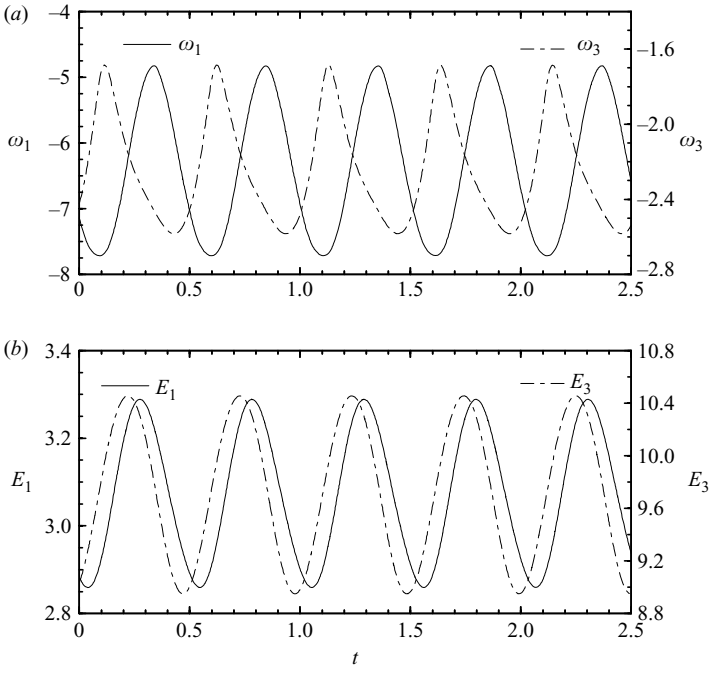


FIGURE 18. Time series of (*a*) precession frequencies and (*b*) kinetic energies of the $m = 1$ and $m = 3$ azimuthal components of QP at $R = 1.85 \times 10^4$ and $F = 0.30$.

The precession frequencies of the Fourier modes $m = 1$ and 3 of the quasi-periodic solutions QP (measured using the technique described at the end of § 2) change in time. This is because a QP solution is no longer a rotating wave with a constant-in-time precession rate. The interaction between the wall mode and the central plume results in precession frequencies ω_1 and ω_3 varying in time as shown in figure 18(*a*)

https://doi.org/10.1017/S0022112009006193 Published online by Cambridge University Press

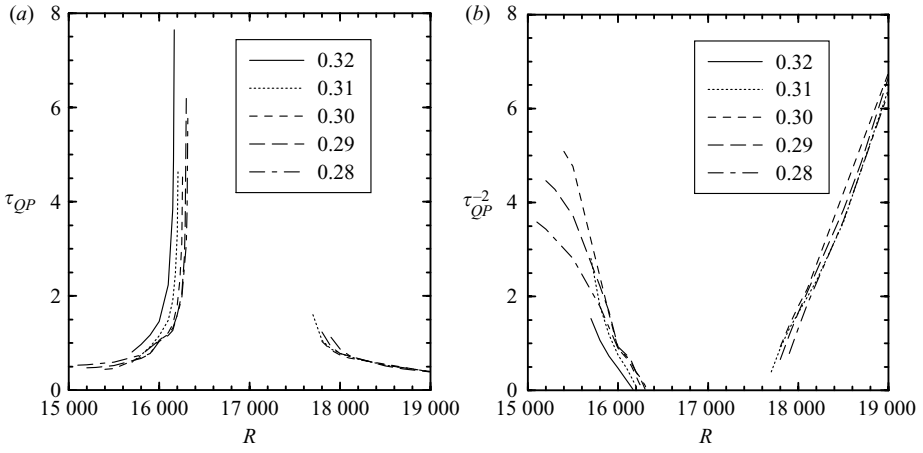


FIGURE 19. (*a*) Variation of the modulation period τ_{QP} with R for various F as indicated; in (*b*) the data is plotted as τ_{QP}^{-2}, showing the typical scaling of the frequency in the neighbourhood of SNIC bifurcations.

for the QP solution at $R = 1.85 \times 10^4$ and $F = 0.30$. The corresponding mean values and variance are $\omega_1 = -6.36 \pm 1.27$ and $\omega_3 = -2.24 \pm 0.75$. Note that the variances are large since the local-in-space precession frequencies are different near the wall and near the axis. The temporal variations in ω_1 and ω_3 are periodic, as illustrated in figure 18(*a*), and both have the same frequency ω_{QP}. Figure 18(*b*) shows the temporal variation in the kinetic energies associated with the Fourier components $m = 1$ and 3 of the same quasi-periodic solution; they have exactly the same frequency ω_{QP}. For a rotating wave, the energies of the Fourier components are constant, but for modulated rotating waves such as QP, they are periodic. This frequency must be an integer multiple of the frequency difference between the two interacting modes, and indeed this is the case here: $\omega_{QP} = 3(\bar{\omega}_3 - \bar{\omega}_1) = 12.36$, where $\bar{\omega}_1$ and $\bar{\omega}_3$ are the time averages of ω_1 and ω_3.

The mean precession frequencies $\bar{\omega}_1$ and $\bar{\omega}_3$ vary substantially in parameter space. When the two precession frequencies approach a rational ratio $\bar{\omega}_1/\bar{\omega}_3 = p/q$, with small integers p and q, the QP state undergoes a SNIC bifurcation leading to a synchronized mixed mode. This is illustrated in figure 19(*a*), showing the period $\tau_{QP} = 2\pi/\omega_{QP}$ as a function of R for different F values. The period goes to infinity at the $SNIC^l$ and $SNIC^u$ bifurcation curves shown in figure 15. Between the SNIC curves, a periodic solution is observed, corresponding to a locking $\omega_1/\omega_3 = 1/3$. Approaching the bifurcation curves, the period goes to infinite following the law $\tau_{QP} \propto |R - R_{crit}|^{-1/2}$, typical of saddle-node bifurcations, as shown in figure 19(*b*).

Typical examples of QP and locked L_{13} states are shown in figure 16. They all look the same because the snapshots lack the temporal evolution information. From the movies available in the online version, it is evident that the $m = 1$ and $m = 3$ components of QP are well-separated spatially on the low-R side of the locking region. On the high-R side of the locking region, the coupling between the $m = 1$ and $m = 3$ components is much stronger. At low R before the $SNIC^l$ bifurcation, during the time evolution, the central plume attaches successively to each of the three plumes close to the wall in a prograde fashion. For the locked mixed mode, the central plume remains attached to one of the wall plumes and the pattern as a whole precesses

https://doi.org/10.1017/S0022112009006193 Published online by Cambridge University Press

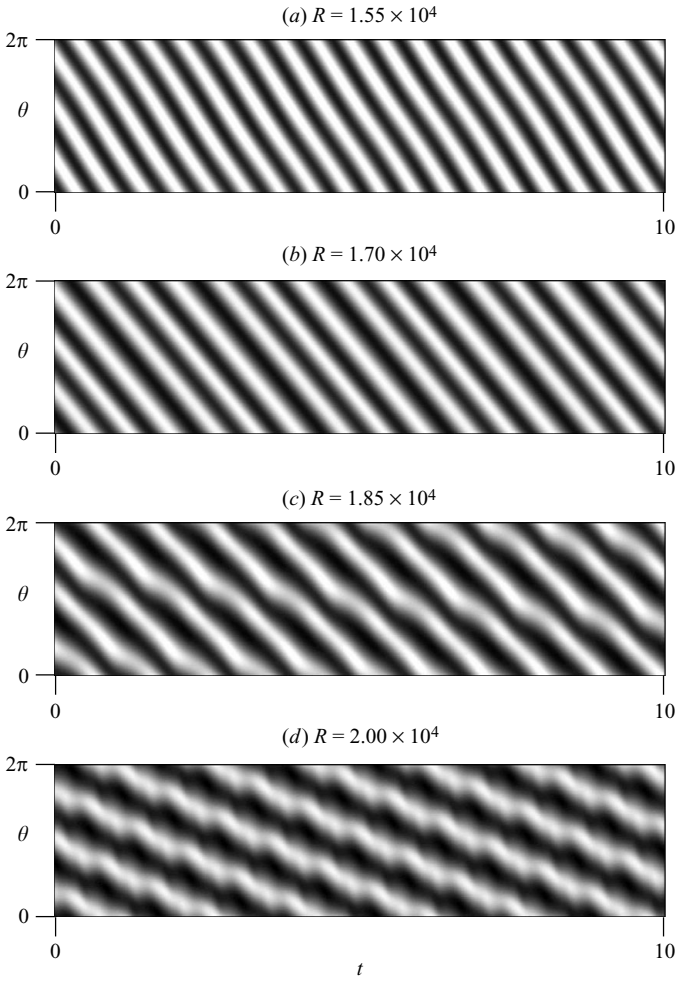


FIGURE 20. Space–time diagram of $\Theta(r = 1, z = 0)$ for the mixed-mode solutions at (*a*) $R = 1.55 \times 10^4$ (QP), (*b*) $R = 1.70 \times 10^4$ (L_{13}), (*c*) $R = 1.85 \times 10^4$ (QP) and (*d*) $R = 2.00 \times 10^4$ (QP), all at $F = 0.30$. The grey scales are from cold (black) to hot (white) in the range $\Theta \in [-0.3, 0]$. The accompanying movies in the online version are animations of these three states, showing contour plots Θ in a horizontal cross-section at mid-height.

uniformly; L_{13} is a rotating wave. For high R, following the $SNIC^u$ bifurcation, the central plume successively attaches to the wall plumes, but now in a retrograde fashion (relative to the global retrograde precession of the wall modes). This behaviour is also evident in the space–time diagrams in figure 20, showing the same four solutions as in figure 16 and in the online movies. These diagrams show the temperature at mid-height on the sidewall as a function of the angle θ (vertical axis) and time (horizontal axis). A vertical cut shows the instantaneous width of the sidewall plumes. Only the locked state in figure 20(*b*) exhibits straight lines, corresponding to the uniform precession of the rotating wave; note that one of the wall plumes is thicker, the one with the central plume attached. The other space–time diagrams show variations in the slope due to the successive attachment of the central plume to alternate sidewall plumes. The effect is most intense at high R. Another salient feature is the reduction

https://doi.org/10.1017/S0022112009006193 Published online by Cambridge University Press

in the mean precession frequency with increasing R, seen as a decrease in the slope in the space–time diagrams. This trend is consistent with the decrease in the precession frequencies of $C3$ and $D3$ as R is increased (see figure 6); the mean precession seen in the space–time diagrams corresponds to the $m=3$ component of the mixed mode which comes from the secondary Hopf bifurcation of $C3/D3$.

Synchronization, or locking, on a 2-torus via a SNIC bifurcation occurs spontaneously in a wide variety of flows, for example, Taylor–Couette (Lopez & Marques 2003; Abshagen *et al.* 2005*a*,*b*, 2008), Rayleigh–Bénard convection (Tuckerman & Barkley 1988), rotating convection (Lopez, Rubio & Marques 2006) and modulated rotating convection (Rubio, Lopez & Marques 2008). While synchronization is often associated with low-order resonance points on the Neimark–Sacker bifurcation curve at which a 2-torus state is born opening up into Arnold's tongues (i.e. resonance horns, regions where the flow on the 2-torus is periodic), this is not the case for the examples just cited, nor for the locked state found here. In fact, the secondary Hopf bifurcation (it is not the generic Neimark–Sacker bifurcation, as QP is a relative periodic orbit bifurcating from relative equilibria, the rotating waves $D1$ and $C3/D3$) cannot have resonance horns emanating from them (Rand 1982; Krupa 1990), and we do not find any such resonances. The synchronization of QP to L_{13}, however, is due to a resonance between the $m=1$ and $m=3$ components of QP, which manifests in a parameter regime where the precession frequencies of the two components are similar. The SNIC curves are far removed in parameter space from the secondary Hopf curves sH_{D1} and sH_{D3}, and the locking region is bounded at high $F\approx0.33$ by a saddle-node bifurcation F_{QL} of limit cycles (inside the locking region) and of 2-tori (outside the locking region).

6. Discussion and conclusion

In this study, we have found a large variety of states and bifurcations. Considering only the stable states, we have found two steady axisymmetric states $C0$ and $D0$, five rotating waves $C2$, $C3$, $D1$, $D3$ and L_{13} and a quasi-periodic solution QP; a total of eight stable states, some of them coexisting, in the explored parameter region $(R, F)=[8\times10^3,\ 2.2\times10^4]\times[0.25,\ 0.60]$. These states appear or change stability at a variety of codimension-one bifurcations, 16 in total. We have also found nine codimension-two bifurcations that act as organizing centres for the dynamics. Two of these bifurcations play an important role: the cusp bifurcation *Cusp*, where the centrifugal and downwelling branches are connected, and the double-Hopf bifurcation dH_{13} of the downwelling branch, which is the origin of the quasi-periodic and locking dynamics. Figure 21(*a*) shows a wide region of the parameter space that includes most of these bifurcations, with the codimension-two points indicated by the symbols •.

With increasing Froude number, the dynamics becomes progressively simpler, and for $F\gtrapprox0.6$ only the steady axisymmetric state $C0$ (the centrifugal branch) remains. In contrast, on decreasing F the complexity of the dynamics increases. In fact, the limit $F\to0$ is problematic, at least in two senses: first, it is not possible to have $F=0$ while keeping a finite value of the Coriolis number Ω, because both numbers have the rotation rate as a factor. The second reason is the increase in complexity of the dynamics as $F\to0$; at larger aspect ratios this results in the chaotic KL dynamics. As such, it is convenient to represent the regime diagram in terms of the inverse Froude number $F^{-1}=Ri$, which is the thermal Richardson number. In this way we obtain figure 21(*b*), showing a simple basic state $C0$ for small R and

https://doi.org/10.1017/S0022112009006193 Published online by Cambridge University Press

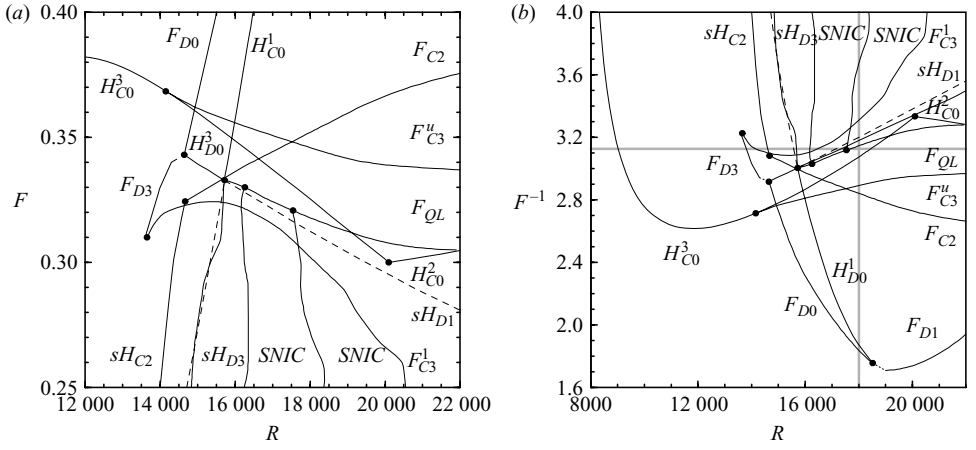


FIGURE 21. (*a*) Bifurcation curves found in the range $(R, F) = [12\,000,\ 22\,000] \times [0.25,\ 0.33]$, and (*b*) the same regime diagram but in terms of F^{-1} for $(R, F^{-1}) = [8 \times 10^3,\ 2.2 \times 10^4] \times [1.6,\ 4.0]$. Bifurcation diagrams for the two one-parameter paths depicted as grey lines in part (*b*) are shown in figure 22.

Ri, and a variety of bifurcations to more and more complex flows on increasing R and Ri.

In order to illustrate the variety of states and the complexity of their bifurcations and interconnections, two one-dimensional paths, one at fixed $R = 1.8 \times 10^4$ and the other at fixed $F = 0.32$, are considered. Figure 22 shows the corresponding bifurcation diagrams along these paths. The $R = 1.8 \times 10^4$ bifurcation diagram (figure 22*a*) shows the centrifugal and downwelling branches, that are clearly separated. $C0$ exists up to $Ri \to 0$, while $D0$ is born at the saddle-node curve F_{D0}. In fact, the two branches remain disconnected on this path until larger values of Ri are reached, where the branches labelled a and b in figure 22(*a*) meet at a saddle-node bifurcation. The bifurcation diagram at $F = 0.32$, shown in figure 22(*b*), displays the complex interconnections between both branches. Here, we also observe two apparently disconnected small branches, in the upper part of the diagram. However, they reconnect at larger R: the two $C3$ branches meet at a saddle-node point beyond the region labelled a, and $C2$ and $C3$ both emerge from the double-Hopf point dH_{23} beyond the region labelled b.

In both bifurcation diagrams, only states computed in this paper and in the previous one (Marques *et al.* 2007) have been displayed; it is very likely that additional unstable branches exist. Note that in both bifurcation diagrams there are regions in parameter space where four different solutions ($D1$, $C2$, $C3$ and QP) coexist and are stable. This multiplicity of coexisting states is typical in small aspect ratio convection; see Hof, Lucas & Mullin (1999) for experiments on non-rotating convection and Boronska & Tuckerman (2006) numerically computed many of these states. The review article Gelfgat & Bar-Yoseph (2004) discusses many issues dealing with multiplicity of states. It is worth noting, however, that in these examples, a primary source of the multiplicity is the presence of symmetries; for example, in the first two cases the symmetry group of the problem is $O(2) \times Z_2$. In our case, there is much less symmetry, only the rotational symmetry around the cylinder axis $SO(2)$, and the multiplicity of states comes about not only from the symmetry but also from the competition between the

https://doi.org/10.1017/S0022112009006193 Published online by Cambridge University Press

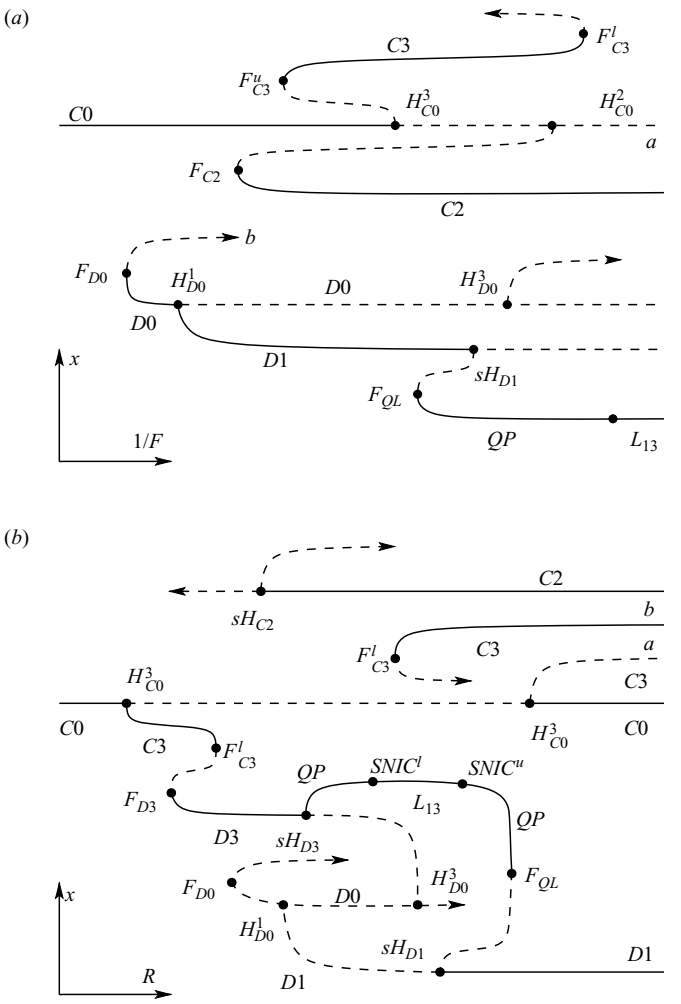


FIGURE 22. Bifurcation diagrams at (*a*) $R = 1.8 \times 10^4$ and (*b*) $F = 0.32$, corresponding to two one-parameter paths through the (R, F) regime diagram, depicted as grey lines, in figure 21.

three independent forces of comparable magnitude in the regime studied: Coriolis, gravitational and centrifugal buoyancies.

Another important fact that is evident from figure 21(*b*) is that for $R \geqslant 1.4157 \times 10^4$ the first bifurcations encountered on increasing the Richardson number $Ri = F^{-1}$ are all subcritical. Therefore, the linear stability analysis of the basic state is not of much use in determining what states will be observed in an experiment. At $R = 2.0 \times 10^4$ for example, linear stability gives that the basic state $C0$ becomes unstable at $Ri \approx 3.32$, whereas there are three additional stable rotating waves that appear at much smaller Ri: D1 at $Ri \approx 1.74$ (saddle-node F_{D1}), $C2$ at $Ri \approx 2.73$ (saddle-node F_{C2}), and $C3$ at $Ri \approx 2.95$ (saddle-node F^u_{C3}).

The solutions we have observed so far, for $F \geqslant 0.25$, are steady states, rotating waves or quasi-periodic solutions with two independent frequencies. This is in contrast with what happens at larger γ in the absence of centrifugal term ($F = 0$), where KL chaotic dynamics is observed. In the present problem, we have computed the solution of the Navier–Stokes equations at $F = 0$ and $R = 2.0 \times 10^4$, using as initial condition

https://doi.org/10.1017/S0022112009006193 Published online by Cambridge University Press

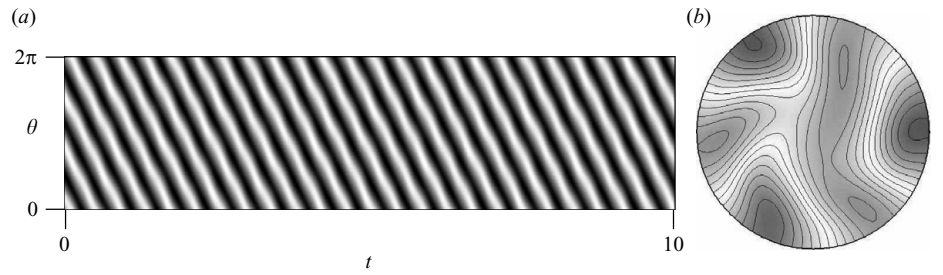


FIGURE 23. (*a*) Space–time diagram of $\Theta(r=1, z=0)$ for $T3$ $R=2.0\times10^4$ at $F=0$. The grey scales are from cold (black) to hot (white) in the range $\Theta\in[-0.31, 0.26]$. (*b*) Snap shot of Θ for $T3$ in a horizontal cross-section at mid-height. The accompanying movie 5 in the online version is an animations of this state.

the QP solution at $F=0.25$ and $R=2.0\times10^4$. The space–time diagram of this solution, $T3$, is presented in figure 23(*a*); since the space–time diagram shows the temperature deviation Θ at the wall, only slight non-periodic deviations from straight lines are observed. In figure 23(*b*), contours of Θ at mid-height are shown, and the accompanying movie 5 in the online version is an animation of this state over 10 thermal times. This state is substantially different from the QP solutions shown in figure 20. The downwelling plume has disappeared, the wall mode plumes penetrate deeper into the interior, and there is a large and almost straight convection roll close to a diameter of the circular section. From the movie, we observe that this roll becomes unstable to another roll at 60°, which in turn becomes unstable to another roll at 60°, and so on. This dynamic is very reminiscent of the KL dynamics reported at larger γ in the limit $Ri\to\infty$ ($F=0$). A detailed analysis of the interplay of the KL dynamics in the bulk and the thermal plumes at the wall for $\gamma=4$ has been recently reported in Marques & Lopez (2008). The dynamic here is similar, but due to the small aspect ratio, only a single convective roll in the interior of the container is observed. Due to this small aspect ratio, we have been able to analyse the variety of states that appear for $F\neq0$ as the number of such states is moderate. At $\gamma=1$ only two stable wall modes have been observed, with azimuthal wavenumbers $m=2$ ($C2$) and $m=3$ ($C3$ and $D3$), whereas for $\gamma=4$ there are 26 Eckhaus–Benjamin–Feir stable wall modes (with $m\in[10, 35]$) that exist before the onset of bulk modes (Lopez *et al.* 2007; Marques & Lopez 2008).

The KL dynamics is chaotic, and in order to see if our state $T3$ also exhibits chaotic behaviour, we have plotted in figure 24 time series of the energies of the first four Fourier modes and the Nusselt number of QP and $T3$. Since QP only has two frequencies, and one is associated to the precession around the cylinder axis, all these functions are periodic for QP. In contrast, the plots for $T3$ show that it has at least one additional frequency; it is a quasi-periodic (or weakly chaotic) state with at least three independent frequencies (a three torus). Table 1 compares the time-averaged values of the five quantities depicted in figure 24 for $T3$, QP and also for the rotating waves $C2$ and $D1$ and the basic (steady and axisymmetric) state $C0$, all at the same Rayleigh number $R=2.0\times10^4$, but differing F. This table shows that the energy shifts from the $m=0$ mode (axisymmetric component), which is dominant at large F, towards the non-zero modes on decreasing F; the non-axisymmetric modes are strongly dominant at $F=0$. The heat flux is also reduced with increasing Froude number. This further supports the conclusions drawn from the results presented in this paper, and summarized in figure 21, that centrifugal effects primarily lead

https://doi.org/10.1017/S0022112009006193 Published online by Cambridge University Press

	$T3$: $F=0$	QP: $F=0.3$	$C2$: $F=0.35$	$D1$: $F=0.35$	$C0$: $F=0.4$
E_0	34.77 ± 5.40	212.4 ± 3.3	263.6	268.2	357.8
E_1	2.35 ± 0.84	3.89 ± 0.39	0	4.449	0
E_2	0.318 ± 0.110	0.692 ± 0.418	13.462	0.0959	0
E_3	66.67 ± 1.17	10.13 ± 0.36	0	0.0013	0
Nu	1.379 ± 0.0165	1.0838 ± 0.0163	1.1306	1.0805	1.049

TABLE 1. Table comparing $T3$, QP, $C2$, $D1$ and $C0$, showing the mean $\pm$ standard deviations in the time-dependent energies of the first four Fourier modes and the Nusselt number, all at $R=2.0\times10^4$ and F as indicated (note that $C0$ is a steady state and $C2$ and $D1$ are rotating waves, so that their energies and Nu are constant).

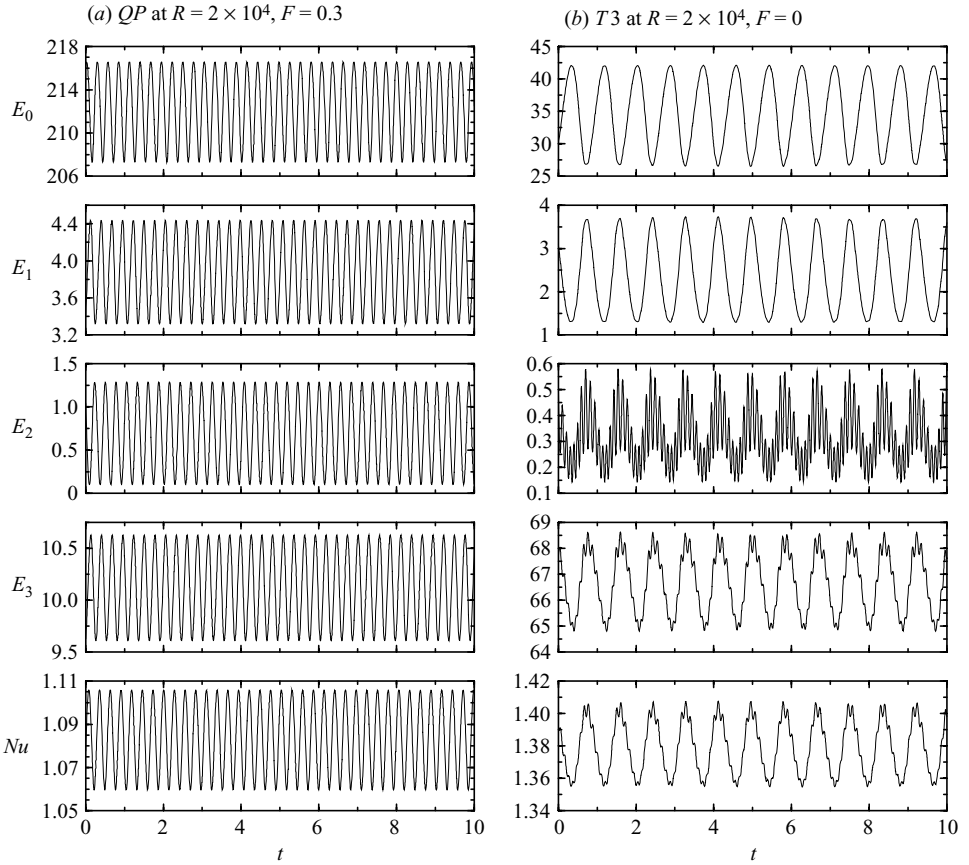


FIGURE 24. Time series of the energies of the first four Fourier modes E_0, E_1, E_2 and E_3, and the Nusselt number Nu of (*a*) QP at $F=0.3$ and (*b*) $T3$ at $F=0$, both at $R=2\times10^4$.

to the axisymmetrization of the flow in regimes where the centrifugal buoyancy dominates.

This work was supported by the National Science Foundation grant DMS-05052705, the Spanish Government grant FIS2007-61585 and Catalonian Government grant SGR-00024.

https://doi.org/10.1017/S0022112009006193 Published online by Cambridge University Press

Appendix. Notation for states and bifurcations

States

Name	Branch	Description
$C0$	Centrifugal	Steady axisymmetric
$C2$	Centrifugal	Rotating wave $m=2$ wall mode
$C3$	Centrifugal	Rotating wave $m=3$ wall mode
$D0$	Downwelling	Steady axisymmetric
$D1$	Downwelling	Rotating wave $m=1$ bulk mode
$D3$	Downwelling	Rotating wave $m=3$ wall mode
QP	Downwelling	Quasi-periodic mixed mode $m=1$ & 3
L_{13}	Downwelling	Rotating wave mixed mode $m=1$ & 3
$T3$	—	Quasi-periodic (or weakly chaotic) with at least three independent frequencies

Codimension-one bifurcations

Name	Description
F_{D0}	Fold of $D0$
F_{D1}	Fold of $D1$
F_{D3}	Fold of $D3$
F_{C2}	Fold of $C2$
F^{l}_{C3}	Fold of $C3$, lower branch
F^{u}_{C3}	Fold of $C3$, upper branch
F_{QL}	Fold of QP or L_{13}
H^{2}_{C0}	Hopf $C0 \rightarrow C2$
H^{3}_{C0}	Hopf $C0 \rightarrow C3$
H^{1}_{D0}	Hopf $D0 \rightarrow D1$
H^{3}_{D0}	Hopf $D0 \rightarrow D3$
sH_{C2}	Secondary Hopf $C2$
sH_{D1}	Secondary Hopf $D1 \rightarrow Q13$
sH_{D2}	Secondary Hopf $D2 \rightarrow Q13$
$SNIC^{l}$	Quasi-periodic $QP \rightarrow$ locking L_{13}, lower branch
$SNIC^{u}$	Quasi-periodic $QP \rightarrow$ locking L_{13}, upper branch

Codimension-two bifurcations

Name	Description
FH_1	Fold-Hopf of $D0$ (F_{D0} and H^{1}_{D0} collide)
FH_3	Fold-Hopf of $D0$ (F_{D0} and H^{3}_{D0} collide)
FH_{C2}	Fold-Hopf of $C2$ (F_{C2} and sH_{C2} collide)
$Cusp$	Cusp bifurcation (F_{D3} & F^{l}_{C3} collide)
dH_{23}	Double-Hopf of $C0$ (H^{2}_{C0} and H^{3}_{C0} collide)
dH_{13}	Double-Hopf of $D0$ (H^{1}_{D0} and H^{3}_{D0} collide)
B	Bautin – degenerate Hopf H^{3}_{C0}
F^{l}_{SNIC}	Fold-SNIC bifurcation ($SNIC^{l}$ and F_{QL} collide)
F^{u}_{SNIC}	Fold-SNIC bifurcation ($SNIC^{u}$ and F_{QL} collide)

https://doi.org/10.1017/S0022112009006193 Published online by Cambridge University Press

REFERENCES

Abshagen, J., Lopez, J. M., Marques, F. & Pfister, G. 2005*a* Mode competition of rotating waves in reflection-symmetric Taylor–Couette flow. *J. Fluid Mech.* **540**, 269–299.

Abshagen, J., Lopez, J. M., Marques, F. & Pfister, G. 2005*b* Symmetry breaking via global bifurcations of modulated rotating waves in hydrodynamics. *Phys. Rev. Lett.* **94**, 074101.

Abshagen, J., Lopez, J. M., Marques, F. & Pfister, G. 2008 Bursting dynamics due to a homoclinic cascade in Taylor–Couette flow. *J. Fluid Mech.* **613**, 357–384.

Barcilon, V. & Pedlosky, J. 1967 On the steady motions produced by a stable stratification in a rapidly rotating fluid. *J. Fluid Mech.* **29**, 673–690.

Barkley, D., Gomes, M. G. & Henderson, R. D. 2002 Three-dimensional instability in flow over a backward-facing step. *J. Fluid Mech.* **473**, 167–190.

Becker, N., Scheel, J. D., Cross, M. C. & Ahlers, G. 2006 Effect of the centrifugal force on domain chaos in Rayleigh–Bénard convection. *Phys. Rev.* E **73**, 066309.

Bodenschatz, E., Pesch, W. & Ahlers, G. 2000 Recent developments in Rayleigh–Bénard convection. *Annu. Rev. Fluid Mech.* **32**, 709–778.

Boronska, K. & Tuckerman, L. S. 2006 Standing and travelling waves in cylindrical Rayleigh–Bénard convection. *J. Fluid Mech.* **559**, 279–298.

Brummell, N., Hart, J. E. & Lopez, J. M. 2000 On the flow induced by centrifugal buoyancy in a differentially-heated rotating cylinder. *Theor. Comput. Fluid Dyn.* **14**, 39–54.

Busse, F. H. 1970 Thermal instabilities in rapidly rotating systems. *J. Fluid Mech.* **44**, 441–460.

Busse, F. H. 1994 Convection driven zonal flows and vortices in the major planets. *Chaos* **4**, 123–134.

Busse, F. H. & Carrigan, C. R. 1974 Convection induced by centrifugal buoyancy. *J. Fluid Mech.* **62**, 579–592.

Busse, F. H., Hartung, G., Jaletzky, M. & Sommerman, G. 1998 Experiments on thermal convection in rotating systems motivated by planetary problems. *Dyn. Atmos. Oceans* **27**, 161–174.

Busse, F. H. & Heikes, K. E. 1980 Convection in a rotating layer: a simple case of turbulence. *Science* **208**, 173–175.

Chandrasekhar, S. 1961 *Hydrodynamic and Hydromagnetic Stability*. Oxford University Press.

Clever, R. M. & Busse, F. H. 1979 Nonlinear properties of convection rolls in a horizontal layer rotating about a vertical axis. *J. Fluid Mech.* **94**, 609–627.

Fornberg, B. 1998 *A Practical Guide to Pseudospectral Methods*. Cambridge University Press.

Gelfgat, A. Y. & Bar-Yoseph, P. Z. 2004 Multiple solutions and stability of confined convective and swirling flows – a continuing challenge. *Intl J. Numer. Methods Heat Fluid Flow* **14**, 213–241.

Goldstein, H. F., Knobloch, E., Mercader, I. & Net, M. 1993 Convection in a rotating cylinder. Part 1. Linear theory for moderate Prandtl numbers. *J. Fluid Mech.* **248**, 583–604.

Goldstein, H. F., Knobloch, E., Mercader, I. & Net, M. 1994 Convection in a rotating cylinder. Part 2. Linear theory for low Prandtl numbers. *J. Fluid Mech.* **262**, 293–324.

Guckenheimer, J. & Holmes, P. 1997 *Nonlinear Oscillations, Dynamical Systems, and Bifurcations of Vector Fields*. Springer.

Hart, J. E. 2000 On the influence of centrifugal buoyancy on rotating convection. *J. Fluid Mech.* **403**, 133–151.

Hof, B., Lucas, P. G. & Mullin, T. 1999 Flow state multiplicity in convection. *Phys. Fluids* **11**, 2815–2817.

Homsy, G. M. & Hudson, J. L. 1969 Centrifugally driven thermal convection in a rotating cylinder. *J. Fluid Mech.* **35**, 33–52.

Homsy, G. M. & Hudson, J. L. 1971 Centrifugal convection and its effect on the asymptotic stability of a bounded rotating fluid heated from below. *J. Fluid Mech.* **48**, 605–624.

Hu, Y., Ecke, R. E. & Ahlers, G. 1997 Convection under rotation for Prandtl numbers near 1: linear stability, wave-number selection, and pattern dynamics. *Phys. Rev.* E **55**, 6928–6949.

Hu, Y., Pesch, W., Ahlers, G. & Ecke, R. E. 1998 Convection under rotation for Prandtl numbers near 1: Küppers–Lortz instability. *Phys. Rev.* E **58**, 5821–5833.

Hughes, S. & Randriamampianina, A. 1998 An improved projection scheme applied to pseudospectral methods for the incompressible Navier–Stokes equations. *Intl J. Numer. Methods Fluids* **28**, 501–521.

https://doi.org/10.1017/S0022112009006193 Published online by Cambridge University Press

Julien, K., Legg, S., McWilliams, J. & Werne, J. 1996 Rapidly rotating turbulent Rayleigh–Bénard convection. *J. Fluid Mech.* **322**, 243–273.

Koschmieder, E. L. 1993 *Bénard Cells and Taylor Vortices*. Cambridge University Press.

Krishnamurti, R. 1971 On the transition to turbulent convection. In *Eighth Symposium on Naval Hydrodynamics*, vol. ARC-179, pp. 289–310. Office of Naval Research.

Krupa, M. 1990 Bifurcations of relative equilibria. *SIAM J. Math. Anal.* **21**, 1453–1486.

Küppers, G. 1970 The stability of steady finite amplitude convection in a rotating fluid layer. *Phys. Lett.* A **32**, 7–8.

Küppers, G. & Lortz, D. 1969 Transition from laminar convection to thermal turbulence in a rotating fluid layer. *J. Fluid Mech.* **35**, 609–620.

Kuznetsov, Y. A. 2004 *Elements of Applied Bifurcation Theory*, 3rd ed. Springer.

Lopez, J. M. & Marques, F. 2003 Small aspect ratio Taylor–Couette flow: onset of a very-low-frequency three-torus state. *Phys. Rev.* E **68**, 036302.

Lopez, J. M., Marques, F., Mercader, I. & Batiste, O. 2007 Onset of convection in a moderate aspect-ratio rotating cylinder: Eckhaus–Benjamin–Feir instability. *J. Fluid Mech.* **590**, 187–208.

Lopez, J. M., Marques, F. & Sanchez, J. 2001 Oscillatory modes in an enclosed swirling flow. *J. Fluid Mech.* **439**, 109–129.

Lopez, J. M., Marques, F. & Shen, J. 2004 Complex dynamics in a short annular container with rotating bottom and inner cylinder. *J. Fluid Mech.* **51**, 327–354.

Lopez, J. M., Rubio, A. & Marques, F. 2006 Traveling circular waves in axisymmetric rotating convection. *J. Fluid Mech.* **569**, 331–348.

Marques, F. & Lopez, J. M. 2008 Influence of wall modes on the onset of bulk convection in a rotating cylinder. *Phys. Fluids* **20**, 024109.

Marques, F., Mercader, I., Batiste, O. & Lopez, J. M. 2007 Centrifugal effects in rotating convection: axisymmetric states and three-dimensional instabilities. *J. Fluid Mech.* **580**, 303–318.

Mercader, I., Net, M. & Falqués, A. 1991 Spectral methods for high order equations. *Comput. Methods Appl. Mech. Engng* **91**, 1245–1251.

Niemela, J. J. & Donnelly, R. J. 1986 Direct transition to turbulence in rotating Bénard convection. *Phys. Rev. Lett.* **57**, 2524–2527.

Ning, L. & Ecke, R. E. 1993 Rotating Rayleigh–Bénard convection: aspect-ratio dependence of the initial bifurcations. *Phys. Rev.* E **47**, 3326–3333.

Nore, C., Tuckerman, L. S., Daube, O. & Xin, S. 2003 The 1:2 mode interaction in exactly counter-rotating von Kármán swirling flow. *J. Fluid Mech.* **477**, 51–88.

Orszag, S. A. & Patera, A. T. 1983 Secondary instability of wall-bounded shear flows. *J. Fluid Mech.* **128**, 347–385.

Ponty, Y., Passot, T. & Sulem, P. L. 1997 Pattern dynamics in rotating convection at finite Prandtl number. *Phys. Rev.* E **56**, 4162–4178.

Portegies, J. W., Kunnen, R. P. J., van Heijst, G. J. F. & Molenaar, J. 2008 A model for vortical plumes in rotating convection. *Phys. Fluids* **20**, 066602.

Rand, D. 1982 Dynamics and symmetry. Predictions for modulated waves in rotating fluids. *Arch. Ratio. Mech. Anal.* **79**, 1–38.

Rossby, H. T. 1967 A study of Bénard convection with and without rotation. *J. Fluid Mech.* **29**, 673–690.

Rubio, A., Lopez, J. M. & Marques, F. 2008 Modulated rotating convection: radially traveling concentric rolls. *J. Fluid Mech.* **608**, 357–378.

Sanchez, J., Marques, F. & Lopez, J. M. 2002 A continuation and bifurcation technique for navier-stokes flows. *J. Comput. Phys.* **180**, 78–98.

Scheel, J. D. 2007 The amplitude equation for rotating Rayleigh–Bénard convection. *Phys. Fluids* **19**, 104105.

Tu, Y. & Cross, M. C. 1992 Chaotic domain structure in rotating convection. *Phys. Rev. Lett.* **69**, 2515–2518.

Tuckerman, L. S. & Barkley, D. 1988 Global bifurcation to traveling waves in axisymmetric convection. *Phys. Rev. Lett.* **61**, 408–411.

Wittenberg, R. W. & Holmes, P. 1997 The limited effectiveness of normal forms: a critical review and extension of local bifurcation studies of the Brusselator PDE. *Physica* D **100**, 1–40.

Zhong, F., Ecke, R. & Steinberg, V. 1993 Rotating Rayleigh–Bénard convection: asymmetric modes and vortex states. *J. Fluid Mech.* **249**, 135–159.

https://doi.org/10.1017/S0022112009006193 Published online by Cambridge University Press